Ocean Sci., 22, 3771–3793, 2026
https://doi.org/10.5194/os-22-3771-2026
© Author(s) 2026. This work is distributed under
the Creative Commons Attribution 4.0 License.

Ocean Science Open Access EGU

First global assessment of the Eddy-Diffusivity Mass-Flux (EDMF) parameterization for oceanic convection in NEMO: implications for global temperature and surface heat fluxes

Violaine Piton[1], **Hervé Giordani**[2], **Romain Bourdallé-Badie**[1], **and Charles Pelletier**[3]

[1]Mercator Ocean International, Toulouse, France
[2]CNRM/CNRS, UMR-3589, Météo-France, Toulouse, France
[3]European Centre for Medium-Range Weather Forecasts, Bonn, Germany

Correspondence: Violaine Piton (vpiton@mercator-ocean.fr)

Received: 3 February 2026 – Discussion started: 5 February 2026
Revised: 9 November 2026 – Accepted: 9 November 2026 – Published: 19 November 2026

Abstract. The Eddy-Diffusivity Mass-Flux (EDMF) parameterization provides a unified framework to represent both local (diffusive) and non-local (convective) vertical mixing in the ocean. While EDMF has been evaluated in idealized and regional configurations, its performance in global ocean models has not yet been assessed. We present the first global-scale evaluation of the EDMF scheme implemented in NEMO and compare it with the widely used Enhanced Vertical Diffusion (EVD) and Mixed Layer Penetration (MLP) parameterizations. Three global 1/4° simulations for 1999–2020 are analyzed, focusing on convective regimes, upper-ocean temperature and mixed-layer depth.

EDMF successfully reproduces both shallow diurnal convection in the tropics and deep wintertime convection in subpolar regions, with modelled plume timing, penetration depth and vertical velocities consistent with available observations. In the tropics, EDMF captures the observed penetrative cooling and depth variability of nocturnal cold plumes, in contrast to the instantaneous adjustment produced by EVD. In deep-convection regions such as the Labrador Sea, EDMF simulates realistic interannual variability in convective depth and intensity. The improved representation of convective regimes leads to a $\sim 30\,\%$ reduction in global upper-ocean (0–700 m) temperature biases in EDMF compared to EVD-based simulations. Changes in latent heat loss, driven by SST differences, dominate the associated changes in net surface heat flux between EDMF and EVD simulations, corresponding to $\sim 6.5\,\%$ of the global average net climatological surface heat balance.

These findings demonstrate that EDMF provides a more physically consistent representation of oceanic convection and offers an alternative to traditional and empirical EVD- and MLP- based approaches.

1 Introduction

By communicating heat, mass and momentum between the atmosphere and ocean interior, the ocean boundary layer (OBL) plays a central role in the evolution of the global ocean heat budget, water-mass formation and air–sea carbon exchange. Vertical mixing within the OBL is typically categorized into two regimes: (i) diffusive mixing, driven by small-scale eddies that transports properties down their local mean gradient, and (ii) non-diffusive mixing, associated with organized large-scale eddies such as convective plumes, which can induce counter-gradient and non-local transport.

Convective plumes are often triggered by surface water cooling or salinification, which can generate hydrostatic instabilities (e.g. increase in surface water density), resulting in downward motion of buoyant plumes. Depending on factors such as the strength of the buoyancy forcing and the ocean stratification, these convective plumes may remain confined to the mixed layer or penetrate to abyssal depths. The forcing also determines the timescales of convective events, which can range from diurnal to seasonal or even interannual (Marshall and Schott, 1999; Morales Maqueda et al., 2004; Vreugdenhil and Gayen, 2021). In tropical and subtropical regions,

daytime solar heating generates a warm, stably stratified surface layer in the upper few meters. At night, surface cooling, often coupled with wind forcing, destabilizes the upper ocean and initiates convective overturning that erodes the diurnal warm layer (Woolnough et al., 2007; Bellenger and Duvel, 2009; Moum et al., 2023). These nocturnal convective plumes are typically shallow, extending only a few tens of meters, with deepest penetrations near the equator (Masich et al., 2021; Moum et al., 2023; Wenegrat and McPhaden, 2015). At higher latitudes, intense surface heat loss during winter drives deep convection events that can reach depths of several hundred to thousand meters. Recurrent wintertime deep convection sites have been identified in the Greenland, Labrador, and Irminger Seas (Våge et al., 2009; Frajka-Williams et al., 2014; Piron et al., 2017), as well as in the Weddell Sea (Gordon, 1978) and the Mediterranean Sea (Schott et al., 1996; Houpert et al., 2016).

By generating large-scale non-diffusive mixing, these two distinct convective regimes (shallow diurnal and deep seasonal) significantly deepen and sustain the upper-ocean mixed layer (Vreugdenhil and Gayen, 2021). Accurately representing convection occurring in the OBL in general circulation models (GCMs) is therefore essential for reliable representation of the mixed layer depth (MLD), and consequent implications on heat storage and global water-mass transport (Fox-Kemper et al., 2019).

For an accurate representation of the total turbulent fluxes within the OBL, both contributions of the diffusive and non-diffusive mixing must be represented. However, the small horizontal scales of the diffusive (O($\sim$ 1–10) m) and non-diffusive (O($\sim$ 10–1000) m) turbulent mixing can not be explicitly resolved in ocean GCMs, as these processes acting primarily in the vertical direction occur at subgrid scales, and therefore must be parameterized. The traditional way to parameterize the turbulent diffusive mixing in GCMs is through the Eddy-Diffusivity (ED) based on a K-gradient approach (Gaspar et al., 1990). This latter estimates the vertical turbulent flux of a field ψ as $\overline{w'\psi'} = -K_z \frac{\partial \psi}{\partial z}$, where K_z ($m^2\,s^{-1}$) is the ED coefficient. Although the ED approach is well suited to representing local diffusive mixing, it cannot explicitly represent the non-local transport associated with large convective eddies, for which the transport can occur independent of the local gradient.

In order to include the non-diffusive mixing, several modifications were introduced into ED formulations. For example, Large et al. (1994) added the effect of non-diffusive convective mixing to the local K-theory through a non-local term (KPP), though many studies discussed biases in KPP due to lack of energetics (Zhu and Zhang, 2019) and its sensitivity to vertical resolutions (Li et al., 2019) and numerical implementation (Van Roekel et al., 2018). An exhaustive and descriptive inventory is provided by Garanaik et al. (2024), though none of these schemes explicitly represent convective plumes as coherent transporting structures. This is also the case for the Enhanced Vertical Diffusion (EVD) parameterization traditionally used in the NEMO ocean model. This approach mimics convective mixing by artificially enhancing vertical diffusivity by assigning large K_z values wherever static instability is detected in the density profile, thereby representing convection as very strong local turbulent vertical diffusion (Madec and the NEMO System Team, 2026). In NEMO, the EVD parameterization is commonly activated along with the mixed-layer penetration (MLP) parameterization which accounts for the effects of near-inertial wave breaking (Fer, 2014) by adding a source of turbulent kinetic energy in the mixed-layer (Rodgers et al., 2014). Used jointly, EVD and MLP have been shown to improve the representation of MLD, near-surface temperature and salinity, and sea ice in the Southern Ocean (Heuzé et al., 2015; Storkey et al., 2018), as well as wintertime MLD in the Arctic region (Allende et al., 2024). However, these improvements can depend on the choice of MLP parameters, which may require regional tuning to reproduce the characteristics of specific convective regimes (Storkey et al., 2018; Allende et al., 2024). At the global scale, Calvert and Siddorn (2013) reported reductions in SST and MLD biases in the extratropical ocean when MLP was included, while highlighting uncertainties associated with the choice of MLP parameters. Lellouche et al. (2021) reported that a seasonal temperature bias remains in the upper ocean of the global ocean reanalysis GLORYS12 despite data assimilation, which they associated with a potential error in stratification above 100 m that may be attributed to the EVD + MLP parameterization. Importantly, Storkey et al. (2018) described the use of MLP as a "stopgap solution" to compensate for underestimated mixing processes in their model (UK Global Ocean GO6 configuration), and highlighted the need for more physically based parameterizations in future model developments. This raises the question of whether the improvements obtained with MLP can instead be achieved through a more physically based representation of convective transport. This motivates the use of a parameterization that explicitly represents the non-local transport associated with convective plumes, rather than approximating its effects through enhanced local diffusivity and TKE.

In this context, the Eddy-Diffusivity and Mass-Flux (EDMF) parameterization was recently introduced in NEMO (Giordani et al., 2020). EDMF unifies a local downgradient diffusive component (ED) with an explicit non-local mass-flux (MF) component that represents the vertical advective transport associated with convective plumes. As such, EDMF has attracted increasing attention as a promising alternative for representing oceanic convection in coarse-resolution models. The EDMF parameterization within NEMO has already been tested and validated in 1-D scenarios within the Gulf of Lions (Mediterranean Sea) and at the PAPA station (northern Pacific Ocean) (Giordani et al., 2020), and in 3-D regional scenarios in the Maud Rise region (off the north coasts of Antarctica) (Gülk et al., 2024). In particular, Gior-

dani et al. (2020) showed that EDMF can reproduce the observed depth and intensity of convective mixing in both moderate and strong convection test cases, providing a basis for evaluating its behaviour in a global configuration. Similar mass-flux-based mixing schemes have also been represented and evaluated in single column test cases (Garanaik et al., 2024, Perrot et al., 2024; Perrot and Lemarié, 2025) or implemented in the code Oceananigans (Ramadhan et al., 2020).

However, the behaviour of EDMF in an idealized 1D framework does not necessarily translate directly to a realistic 3D ocean. In the 1D experiments of Giordani et al. (2020), horizontal advection and the associated redistribution of water masses are neglected, allowing vertical mixing processes to be isolated but preventing the assessment of their interaction with the 3D ocean circulation. A global 3D simulation is therefore a necessary complementary step to assess whether the benefits identified in 1D persist in a realistic ocean and to examine their consequences across a range of spatial and temporal scales. To the best of our knowledge, the EDMF parameterization has not previously been evaluated in a global ocean model configuration.

Under the framework of the NEMO Consortium, which ensures the sustainable development of the NEMO platform to support oceanographic research, forecasting, and climate studies, this paper has four main objectives:

- To evaluate the EDMF parameterization in a global NEMO simulation at $1/4°$ resolution, by assessing key variables such as temperature, salinity, ocean transport, and mixed layer depth (MLD);
- To compare the performance of the EDMF scheme against two widely-used EVD-based parameterizations, with and without the empirical MLP formulation, in representing the aforementioned variables;
- To assess the ability of the EDMF scheme to represent two contrasting convective regimes, from shallow tropical diurnal convection to seasonal deep convection in the North Atlantic, and to examine their effects on OBL dynamics;
- To quantify the contribution of convection to the global net surface fluxes, from regional to global scales.

The remainder of the paper is organized as follows. Section 2 describes the model configuration and the vertical mixing parameterizations used in our three experiments. Section 3 first evaluates the performance of EDMF in representing two distinct convective regimes and then examines its impact on temperature and MLD patterns relative to the EVD and state-of-the-art EVD + MLP simulation. Section 4 assesses the contribution of the mass-flux component to surface heat fluxes. Finally, Sect. 5 presents the discussion and concluding remarks.

2 Methods

2.1 Model and simulations performed: shared features

We analyze the outputs of three NEMO standalone simulations which differ one from another only by their respective choice of vertical diffusive and/or convection parameterizations. In this subsection, we describe the experimental design shared by all three experiments.

We use the ocean-sea ice coupled model of the Nucleus for European Modelling of the Ocean (NEMO) version 4.2 (Madec et al., 2022), coupled with the Sea Ice modelling Integrated Initiative (SI3, Vancoppenolle et al., 2023), with its default settings and five ice thickness categories. Simulations are performed on a $1/4°$ global tripolar grid with 75 vertical ocean z levels, with local thickness starting at 1 m at the surface, and increasing up to 200 m near the bottom of the model ocean. Atmospheric forcing is provided by the ERA5 reanalysis at hourly frequency (Hersbach et al., 2020) via the IFS bulk formula (Brodeau et al., 2017). The Gent–McWilliams (GM) parameterization of eddy-induced velocities (Gent and McWilliams, 1990) is activated consistently across all simulations, using the formulation of Treguier et al. (1997) with a lateral diffusive velocity of $0.01\,\mathrm{m\,s^{-1}}$ and a lateral diffusive length scale of 200 km, corresponding to a maximum mixing coefficient of $1000\,\mathrm{m^2\,s^{-1}}$. Although the GM configuration is identical across all three simulations, interactions between this parameterization and the vertical mixing schemes may occur. A detailed investigation of these interactions is beyond the scope of the present study. The penetration of solar radiation is prescribed following the algorithm of Morel (1988). The monthly climatology field of surface chlorophyll of Sathyendranath et al. (2019) is used to compute the light penetration profiles.

All three simulations are conducted over the 1999–2020 period. The ocean and ice fields are initialized on 1 October 1999 using the state-of-the-art Global Reanalysis Ensemble Product (GREP) at $1/4°$ resolution, provided by the Copernicus Marine Service. Following a five-year spin-up period, the model outputs were analyzed over a 16-year period spanning 2005–2020 corresponding to the Argo program period.

2.2 Vertical mixing parameterization options

We now focus more specifically on the parameterization pertaining to vertical mixing. For representing vertical diffusive mixing, all three experiments employ a "1.5th-order" turbulent-kinetic-energy (TKE) closure scheme initially proposed by Blanke and Delecluse (1993). The eddy diffusivity K_z is then diagnosed from the TKE. In one of our simulations (called TKE + MLP + EVD, Table 1), the TKE scheme is complemented with the so-called "mixed-layer penetration" (MLP) scheme, increasing the upper ocean TKE to account for the effects of near-inertial oscillations and surface gravity wave breaking (Rodgers et al., 2014). The

Table 1. Summary of conducted experiments.

Simulation	Diffusion	MLP?	Convection
TKE + EVD	TKE	No	EVD
TKE + MLP + EVD	TKE	Yes	EVD
EDMF	TKE	No	Mass-flux

MLP scheme adds a TKE source term (in our case, 5 % of the surface TKE), distributed vertically with an exponentially decreasing shape function from the surface down to depths ranging from 0.5 m (at the Equator) down to 40 m (at higher latitudes in both hemispheres). Introduced as an ad-hoc empirically-based parameterization, the MLP was implemented to deepen the mixed layer depth (MLD), which was commonly found to be too shallow in the Southern Ocean during summer under windy conditions (Rodgers et al., 2014). This scheme is active by default in NEMO4.2, as it has been shown to improve the realism of MLD in the Southern Ocean, Arctic region and open-water areas (Calvert and Siddorn, 2013; Rodgers et al., 2014; Heuzé et al., 2015; Storkey et al., 2018; Allende et al., 2024).

NEMO's current default option for representing convective vertical mixing is the "enhanced vertical diffusivity" (EVD) parametrization (Madec and the NEMO System Team, 2026). When the stratification between two vertically adjacent cells is unstable (i.e., when the density decreases with depth), the EVD scheme increases the eddy diffusivity by several orders of magnitude, resulting in very large mixing between two vertical grid cells. Under stable stratification, the EVD parameterization leaves K_z unchanged and is thus inactive, whereas under unstable stratification conditions, EVD assigns K_z to $100\,\mathrm{m^2\,s^{-1}}$ in our simulations. In essence, the EVD represents non-local vertical mixing via a fundamentally local mechanism (diffusion, i.e., $K_z\partial_z T$), albeit employing diffusivities large enough to mimic non-local effects. The EVD scheme is used in our experiments called TKE + EVD and TKE + MLP + EVD, further detailed below and in Table 1.

As an alternative to the EVD parameterization, NEMO4.2 now also allows the use of the mass-flux parameterization to represent the convective vertical mixing with a dedicated numerical formulation (see Giordani et al., 2020). Inspired by atmospheric convective parameterizations (Siebesma et al., 2003; Soares et al., 2004), it explicitly represents convective plumes nested within their surrounding environment and is by construction non-local. The mass-flux parametrization aims solely at representing convective mixing and is typically combined with the aforementioned TKE closure, accounting for diffusive mixing. The combination of both parametrizations is hereinafter referred to as Eddy-Diffusivity Mass-Flux (EDMF) parametrization, and is used in our experiment called EDMF (Table 1). EDMF parameterization is designed to respond to density instabilities regardless of their origin, including, for example, those induced by surface cooling or salinification, wind-driven Ekman transport (e.g. Thomas and Lee, 2005), eddy-induced downwelling near the shedding region of cyclonic boundary currents in convective basins (Spall, 2010), or near-inertial oscillations (Fer, 2014). The main characteristics of the mass-flux component of EDMF scheme (Giordani et al., 2020) are briefly recalled here. To estimate the mass-flux, the following variables are estimated: the convective plume covers a fraction a_p of the grid cell, called fractional area, representing the probability of convection occurrence in a grid-cell and has conservative properties $\psi_\mathrm{p} = (T_\mathrm{p}, S_\mathrm{p})$ and a downward velocity w_p, whereas the surrounding environment has conservative properties $\psi = (T, S)$, which are the prognostic variables of the model. In the present implementation, the mass-flux scheme is applied only to tracers and does not affect the momentum field. The computation of w_p is done by integrating the equation:

$$\left(\frac{1}{2}+\alpha\right)\frac{\partial w_\mathrm{p}^2}{\partial z} = a_1 F_\mathrm{b} - \alpha g \frac{\rho_\mathrm{p}}{p_\mathrm{h}} w_\mathrm{p}^2, \tag{1}$$

where g is the gravitational acceleration, F_b is the plume buoyancy acceleration, ρ_p is the surface-referenced potential density of the plume, p_h is the hydrostatic pressure, and a_1 and α are the coefficients. The value $a_1 = 1$ was diagnosed from Large Eddy Simulations in the atmosphere (Siebesma et al., 2003) and $\alpha = 0.2$ was found to produce the best results in 1-D EDMF test cases (Giordani et al., 2020). However, the parameter α was assigned a different value from that used by Giordani et al. (2020), whose calibration was based on only two 1-D cases. Preliminary global tests (not discussed in this paper) showed that setting $\alpha = 1$ yielded more realistic results, particularly in the tropical region. These tests also showed that the values of the other parameters introduced below (i.e. β_1, β_2 and ϵ_g) could be retained from the calibration of Giordani et al. (2020).

The surface buoyancy flux is used to derive the fractional convective area of a plume at the surface using a closure derived from Grant (2001) and Pergaud et al. (2009) (see Giordani et al., 2020, for details). Below the surface, the computation of a_p is determined as:

$$\frac{1}{a_\mathrm{p}}\frac{\partial a_\mathrm{p}}{\partial z} = -\mathcal{L} + \epsilon_{a_\mathrm{p}} - \delta_{a_\mathrm{p}} \text{ with } \mathcal{L} = \frac{1}{w_\mathrm{p}}\frac{\partial w_\mathrm{p}}{\partial z}. \tag{2}$$

These quantities correspond to vertical decay scale, as described in Giordani et al. (2020). Within the convective area, the vertical velocity increases with depth in the upper part of the plume ($\mathcal{L} > 0$) and decreases with depth in the deeper part ($\mathcal{L} < 0$), resulting in maximum vertical velocity at the transition between the two regions.

In Eq. (2), the entrainment (ϵ_{a_p}) and detrainment (δ_{a_p}) rates between the plume and the environment are expressed as:

$$\epsilon_{a_\mathrm{p}} = \beta_1 \mathrm{Max}(0, \mathcal{L}), \tag{3}$$

$$\delta_{a_p} = -\beta_2 \mathrm{Min}(0, \mathcal{L}), \tag{4}$$

with the coefficients $\beta_1 = \beta_2 = 0.9$ (Rio et al., 2010; Giordani et al., 2020).

On the other hand, the plume properties (ψ_p) are determined as:

$$\frac{\partial \psi_p}{\partial z} = -\epsilon_\psi (\psi_p - \psi), \tag{5}$$

with the lateral entrainment rate ϵ_ψ between the plume and the environment computed as:

$$\epsilon_\psi = \left| \frac{1}{w_p} \frac{\partial w_p}{\partial z} \right| + \epsilon_g. \tag{6}$$

For consistency with ϵ_{a_p} and δ_{a_p} (Eq. 3), we introduce a coefficient β in the computation of ϵ_ψ so that:

$$\epsilon_\psi = \beta \mathrm{Max}(0, \mathcal{L}) + \epsilon_g, \tag{7}$$

with $\beta = \beta_1 = \beta_2 = 0.9$, and the background entrainment rate ϵ_g equal to 0.001 (Giordani et al., 2020; Gülk et al., 2024). Lastly, the initialization of T_p at the surface was originally coded to be equal to the surface temperature of the environment (T) at the same time step. The NEMO version used in this study uses a leapfrog time-stepping scheme. The surface flux is evaluated at the half time step, which allows it to be used at the temporal center of the model time step. To allow convection triggering with $T_p < T$, we modified the initialization so that the surface T_p is now set equal to surface T at the following half time step. This temperature increment is an estimate of the temperature difference between the convective plumes and their surrounding environment in the model grid-mesh. Note that the present EDMF formulation is applied for all convective regimes, without using regime-specific parameterizations or coefficients.

As mentioned above, the vertical mixing parameterization choice distinguishes our three experiments one from another, for which Table 1 provides an overview. In our study, TKE + EVD can be considered as a "minimal" control experiment; TKE + MLP + EVD as a control experiment with settings that NEMO usually employ (including the ad-hoc MLP parametrization); and EDMF is the new framework we are evaluating. The aim of the present study is to improve the representation of the vertical physics in the model, and ultimately, its ability to reduce systematic biases. However, the full potential of the new parameterization may only become apparent after a recalibration of its parameters within the complete model configuration (Hourdin et al., 2021, 2023).

2.3 Observational dataset for simulations evaluation

The modeled sea surface temperature (SST) is compared to SST data from OSTIA (Operational Sea Surface Temperature and Sea Ice Analysis), while the modeled vertical profiles of temperature are compared to in-situ measurements from ARMOR and CORA-REP product. These widely used observational products provide extensive global in-situ coverage and are therefore suitable for evaluating the temperature and salinity fields of the global ocean. The hourly model output is interpolated in space and time to the location and time of each observation. For the vertical profile comparison, the model output is additionally interpolated vertically to the observed depth levels. The resulting model values at the same location, time and depth as the observations are referred to as the "model equivalents of the observations". This approach is commonly used in ocean data assimilation systems, including the GLORYS12 near-real-time operational system (Lellouche et al., 2021). The bias and root mean square deviation (RMSD) are then calculated within $3° \times 3°$ grid boxes to ensure statistical robustness by minimizing the risk of having too few in-situ observations within smaller boxes.

Modeled monthly mixed-layer depth (MLD) climatologies are compared to the MLD climatology of de Boyer Montégut (2024), derived from temperature and salinity profiles collected between January 1970 and December 2021 from the NCEI-NOAA World Ocean Database and ice-tethered profilers, supplemented by data from the Argo program where available. The MLD for each profile is computed using the threshold density criterion, following de Boyer Montégut et al. (2004), consistent with the online MLD computation used in NEMO and the present study. This profile-based MLD has been recommended for the evaluation of global ocean models, such as those partaking in OMIP (Tréguier et al., 2023). The observational climatology has a spatial resolution of $1° \times 1°$, so the modeled MLD climatologies are averaged to this resolution for comparison.

To evaluate the ability of the mixing schemes to represent shallow diurnal convection, which is particularly prevalent in the tropics, we compare modeled hourly near-surface temperatures with in-situ observations from a the standard operational Tropical Atmosphere Ocean (TAO) surface mooring located at 2° S, 140° W and maintained by the National Data Buoy Center (NDBC). The data were collected and made freely available by NOAA/NDBC. From February 2017 to June 2018, this mooring was additionally equipped with temperature sensors providing enhanced vertical resolution, with measurements every 5 m from the surface to 40 m depth and every 10 m between 40 and 60 m depth, at a sampling interval of 10 min. This enhanced vertical resolution makes these observations particularly suitable for evaluating the tropical shallow diurnal convection and associated vertical temperature structure investigated in this study (Masich et al., 2021). For a like-for-like comparison, the observational data were temporally averaged to match the hourly frequency of the model output.

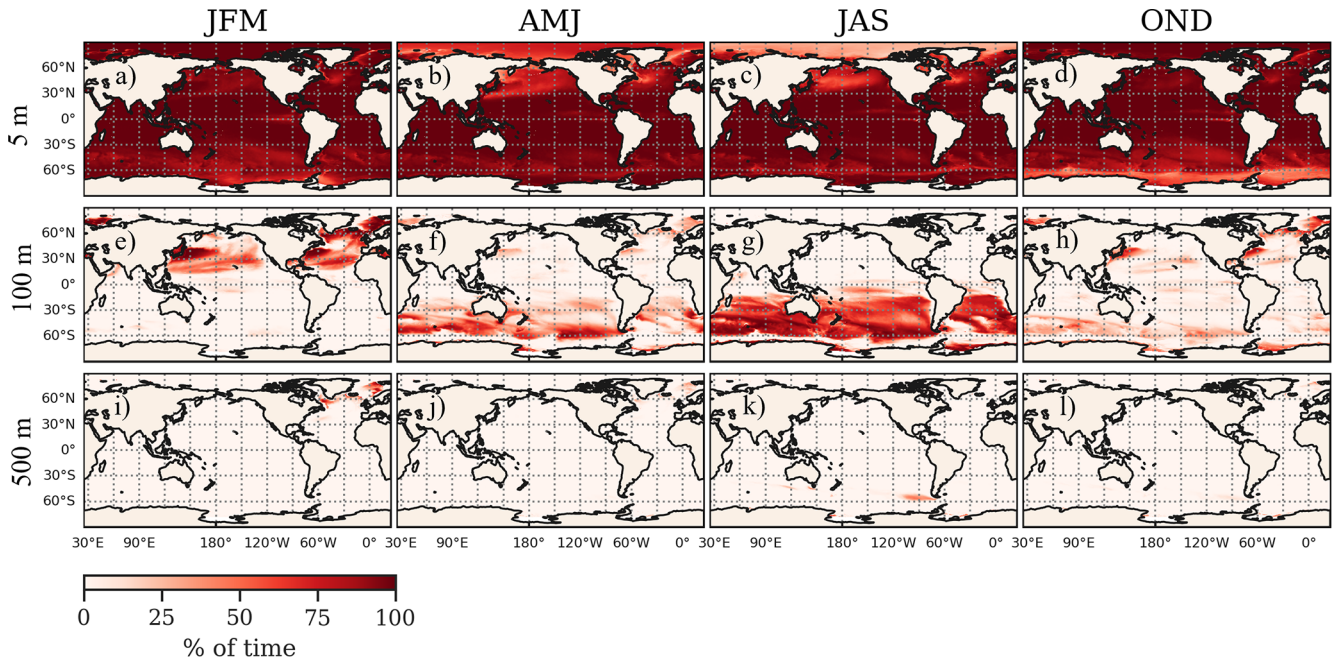


Figure 1. Seasonal activity of the mass-flux component, as depicted as positive values of w_p averaged over the 2005–2020 period, at 5 **(a–d)**, 100 **(e–h)** and 500 m depth **(i–l)** in terms of percentage (%) of time per month.

3 EDMF scheme evaluation

In this section, we first describe the spatio-temporal global occurrences of the EDMF scheme. Second, we evaluate EDMF at two representative locations corresponding to contrasting convective regimes: a site in the Labrador Sea, representative of seasonal deep convection, and a site in the equatorial Pacific, representative of recurrent shallow diurnal convection. These case studies complement the idealized 1D experiments of Giordani et al. (2020) by assessing the behavior of EDMF in a fully 3D ocean with realistic circulation and spatially varying forcing. We then evaluate the performance of the simulation using the EDMF scheme in reproducing observed temperature patterns and MLD cycles at global and regional scales, and we compare its skill to that of the simulations employing the EVD scheme (TKE + EVD and TKE + MLP + EVD simulations). Additional analysis of the EDMF performances in reproducing the Atlantic meridional overturning circulation (AMOC) is available in Sects. S1 and Fig. S8 of the Supplement.

3.1 EDMF scheme occurrence

We assess the occurrence of the mass-flux component of the EDMF scheme by analyzing climatological (2005–2020) fields of daily plume vertical velocities (w_p) outputs from the EDMF simulation, where positive w_p indicate the presence of convective plumes (Fig. 1). These results indicate that the mass-flux component is active year-round in the tropical ocean (30° S–30° N), where it is confined to shallow depths (< 100 m) (Fig. 1a–h). This convective activity is characteristic of the diurnal shallow convective regime that occurs in the tropics and subtropics at night, driven by the combined effects of wind and nighttime surface cooling (Shay and Gregg, 1986). During boreal winter, the mass-flux component is activated in the Northern Hemisphere (Fig. 1e), whereas activation shifts to the Southern Hemisphere during austral winter (Fig. 1g), reflecting the seasonality of convective events. Deep convective activities (> 500 m) are depicted in the northern Atlantic (Labrador and Irminger Seas) and southwestern Pacific near the Drake passage during boreal and austral winter, respectively (Fig. 1i–l). In these regions, seasonal wintertime deep convection has been observed and documented (Yashayaev and Loder, 2017; Behrens et al., 2016).

3.1.1 Deep-seasonal convection

To investigate the performance of EDMF in representing the seasonal deep convection, we focus on the Labrador Sea region. No continual observational time series are directly available in this region. We select the grid cell 56.53° N, 52.65° W as a representative point, analyzing the model outputs at the hourly temporal resolution. We assess the simulated convection against published observations in the region in terms of its timing, depth and intensity, rather than performing a direct point-by-point comparison. Figure 2a presents the time series of surface net heat flux and w_p over four consecutive years (2011–2015). Each year, a gradual deepening and intensification of w_p is observed from late

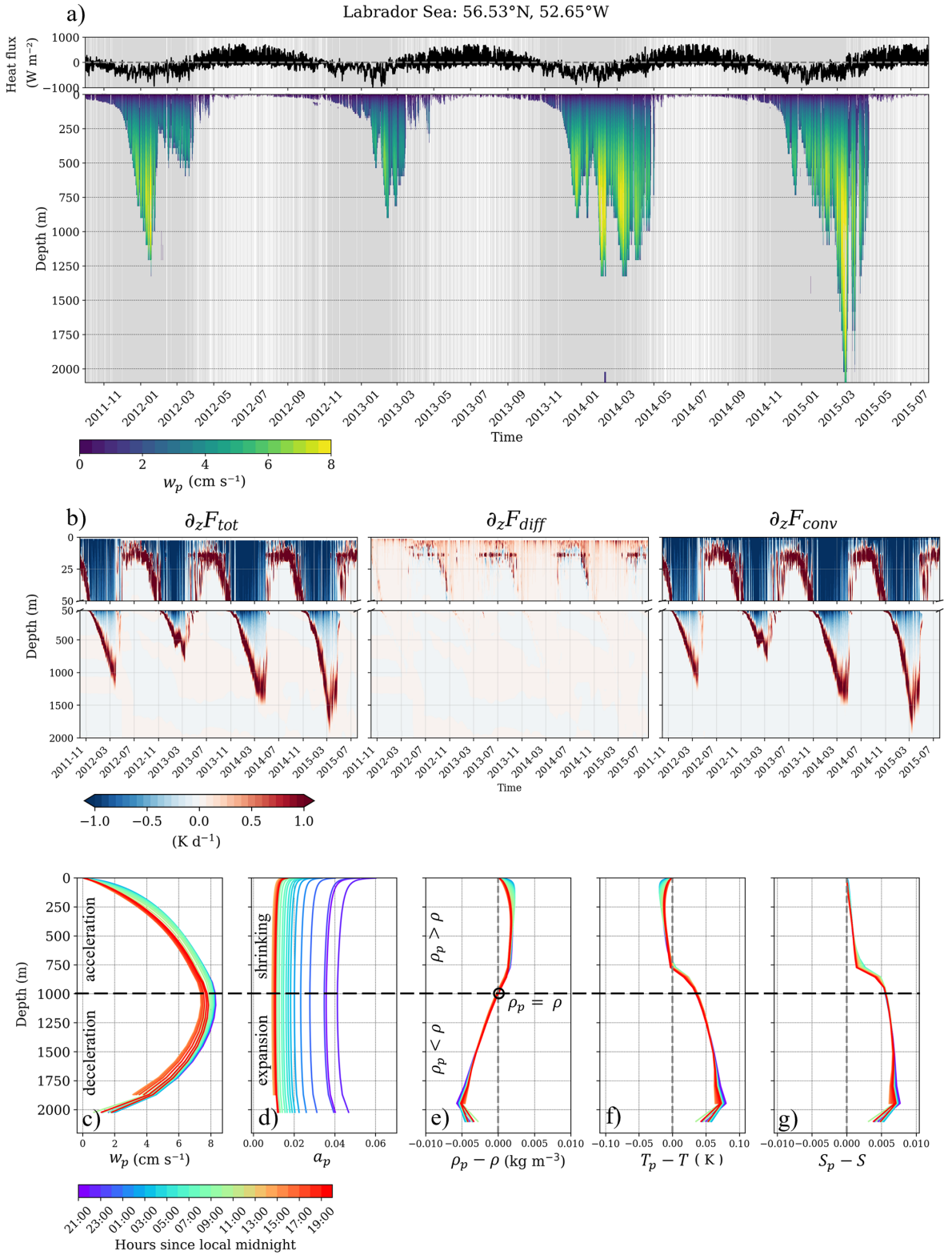


Figure 2. **(a)** Hourly time series of surface net heat flux ($\mathrm{W\,m^{-2}}$) and plume w_p ($\mathrm{cm\,s^{-1}}$) spanning October 2011 to July 2015 at the model grid cell located at 56.53° N, 52.65° W in the Labrador Sea. Vertical gray patches correspond to period of negative heat flux. **(b)** Daily time series of temperature trend ($\mathrm{K\,d^{-1}}$) from the divergence of the total ($\partial_z F_\mathrm{tot}$), diffusive ($\partial_z F_\mathrm{diff}$) and convective ($\partial_z F_\mathrm{conv}$) heat flux from EDMF simulation. 24 h profiles of **(c)** w_p, **(d)** a_p, **(e)** $\rho_\mathrm{p} - \rho$, **(f)** $T_\mathrm{p} - T$ and **(g)** $S_\mathrm{p} - S$ for 15 March 2015. The dashback line denotes the depth of neutral buoyancy between the plume and the environment ($\rho_\mathrm{p} = \rho$).

summer into autumn (August to November), associated with the seasonal transition from positive to negative surface heat flux. As winter progresses (December), the intensification of negative heat flux triggers the onset of deep convection (depths > 500 m), marked by a rapid increase in both depth and magnitude of w_p. The deep convection season typically stops in early spring (April), associated with the transition from negative to positive surface net heat flux.

However, substantial interannual variability in the intensity of the convection is observed (Fig. 2a). During the winter of 2012–2013, the convective season was relatively short (late January to mid-March) and weak, with w_p reaching a maximum depth of ~ 900 m and peak values of $\sim 5\,\mathrm{cm\,s^{-1}}$. In contrast, the winter of 2014–2015 was marked by an early onset of convection (beginning in December), which persisted through mid-April, reaching depths up to ~ 2000 m and $w_p > 8\,\mathrm{cm\,s^{-1}}$. Apart from major convective events, wintertime MLDs observed in the Labrador Sea typically range between 500 and 1500 m (Kieke and Yashayaev, 2015), consistent with the modelled maximum plume depths during the winters of 2011–2012, 2012–2013 and 2013–2014 (Fig. 2a). The winter 2014–2015 has been identified as a major deep convection event, occurring in both the Labrador and Irminger Seas (Piron et al., 2017), with depths comparable to those observed during 1993–1995 of ~ 2300 m (Kieke and Yashayaev, 2015). The modelled convective depths during winter 2014–2015 are consistent with Argo-derived MLDs in the Labrador Sea, which ranged from 1000 to 1800 m during March-April 2015 (Piron et al., 2017). The modelled w_p also fall within the range of the few available observational estimates of w_p, although such observational measurements remain scarce because of the difficulty in sampling small oceanic vertical velocities. Using gliders deployed in the Labrador Sea during winter 2022, Clément et al. (2024) reported maximum w_p of $4.6\,\mathrm{cm\,s^{-1}}$ and MLDs reaching 1000 m. These values indicate moderate convective conditions, consistent with the modelled values for the winter 2011–2012 which presents moderate conditions compared to winters 2012–2013 and 2014–2015 (Fig. 2a).

To analyze the impact of the vertical schemes to the oceanic properties, we choose to use daily model outputs at the model grid cell (56.53° N, 52.65° W) to compute the temperature trend from the divergence of the diffusive ($\partial_z F_{\mathrm{diff}}$), convective ($\partial_z F_{\mathrm{conv}}$) and total ($\partial_z F_{\mathrm{tot}}$) vertical heat fluxes as:

$$\partial_z F_{\mathrm{diff}} = -\frac{\partial}{\partial z}\left(-K_z \frac{\partial T}{\partial z}\right), \tag{8}$$

$$\partial_z F_{\mathrm{conv}} = -\frac{\partial}{\partial z}\left(\frac{\partial a_p w_p (T_p - T)}{\partial z}\right). \tag{9}$$

In the case of EDMF simulation, the total trend for vertical heat fluxes is defined to be: $\partial_z F_{\mathrm{tot}} = \partial_z F_{\mathrm{diff}} + \partial_z F_{\mathrm{conv}}$; whereas in the case of the EVD simulations it is defined as: $\partial_z F_{\mathrm{tot}} = \partial_z F_{\mathrm{diff}}$.

$\partial_z F_{\mathrm{diff}}$ is nearly negligible over most of the water column, except for a weak signal close to the surface during the summers (Fig. 2b). Consequently, the vertical structure of $\partial_z F_{\mathrm{tot}}$ is almost entirely determined by the convective contribution, $\partial_z F_{\mathrm{conv}}$. This illustrates that the deep response of the total vertical heat flux in the EDMF simulation is primarily associated with the mass-flux component rather than with diffusive mixing. Time series of $\partial_z F_{\mathrm{tot}}$ and $\partial_z F_{\mathrm{diff}}$ for the two EVD simulations are provided in Fig. S1 in the Supplement, using the same location and time period, to compare the intensity and vertical extent of these fluxes under the same surface forcing.

Hourly profiles of the modelled convective plumes characteristics for 15 March 2015, are shown in Fig. 2c–g. This date was selected as it falls within the core of the most intense convective winter shown in Fig. 2a. At the surface, negative heat fluxes trigger and maintain colder-than-environment plume temperatures ($T_p < T$, Fig. 2f) throughout, resulting in denser-than-environment plume waters ($\rho_p > \rho$, Fig. 2e). The plume convective areas (a_p), derived from surface buoyancy fluxes, are provided in Fig. 2d. As the plumes propagate downward and remain denser than their environment waters ($\rho_p > \rho$), they accelerate and reach vertical velocities up to $8\,\mathrm{cm\,s^{-1}}$ while their a_p gradually shrink. At the depth of neutral buoyancy – where plume and environment densities become equal ($\rho_p = \rho$), around ~ 1000 m – the plumes begin to decelerate, accompanied by an increase in a_p (their expansion). Below this level, as the plume waters become lighter than the environment waters ($\rho_p < \rho$), the plumes lose their gained buoyancy and eventually stops ($w_p = 0$) at depths of ~ 1700–2000 m.

3.1.2 Shallow-diurnal convection

First, the simulated shallow convective depth range (< 100 m) observed in the tropics (30° S–30° N; Fig. 1a–h) is broadly consistent with observational estimates from the tropical Pacific and Atlantic. Using the TAO mooring array across the tropical Pacific, Masich et al. (2021) reported mean convective depths of 10–60 m, while Moum et al. (2023) reported maximum convective depths of up to 90 m at 0°, 140° W, based on turbulence measurements. In the tropical Atlantic, Moum et al. (2023) reported maximum convective depths of 65 m at 0°, 23° W and 36 m at 0°, 10° W from PIRATA mooring observations. These comparisons provide a first quantitative assessment of the simulated depth range, while a more detailed comparison with observations at the TAO mooring site 2° S, 140° W is presented below.

Second, we apply a similar analysis for the shallow diurnal convection to that presented in Sect. 3.1.1. We select the grid cell located at 2° S, 140° W as representative of the shallow diurnal convection in the equatorial Pacific (Fig. 1a–d) and analyzing hourly model outputs for July 2017. The full-month period is shown to illustrate the

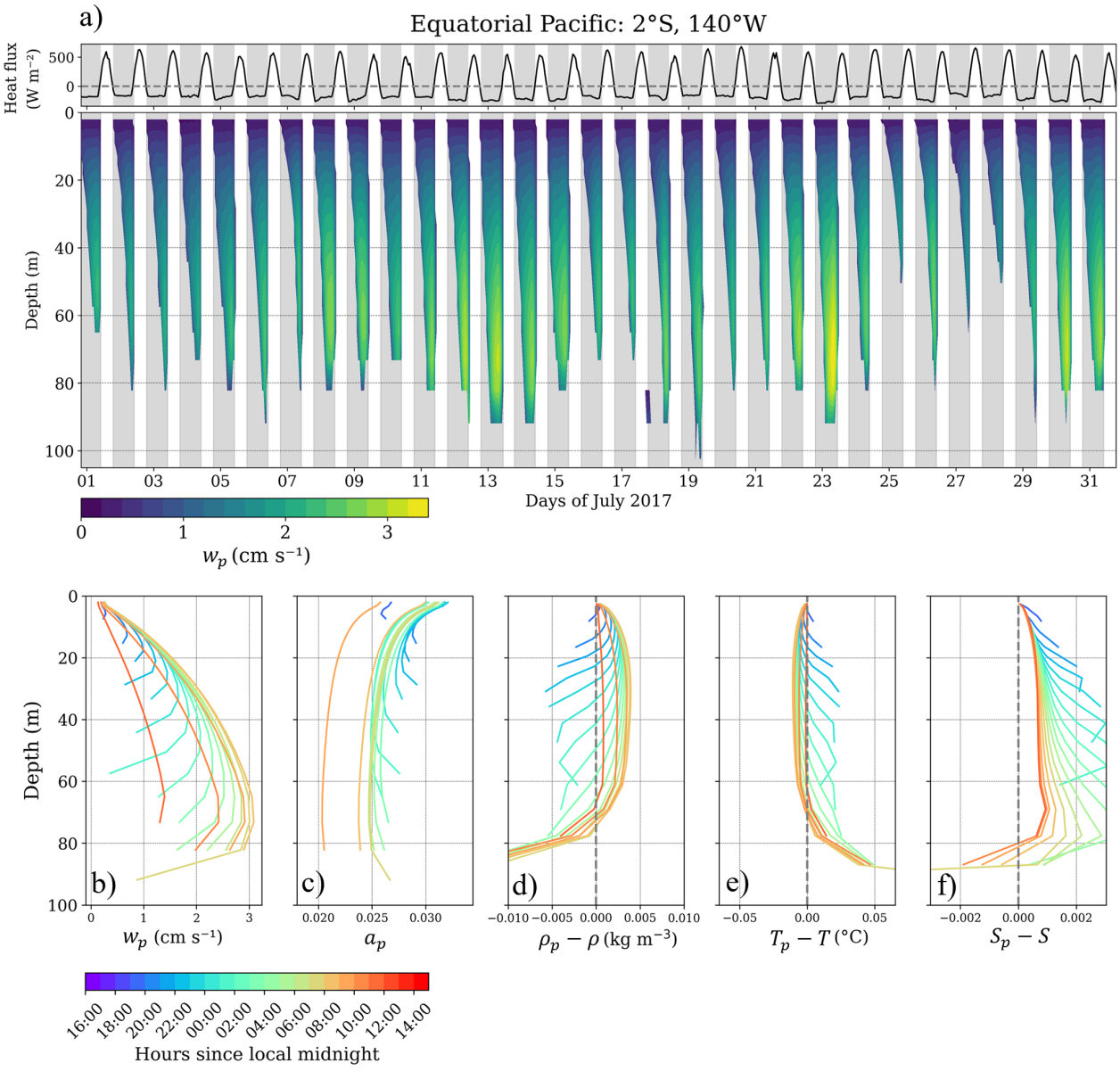


Figure 3. **(a)** Hourly time series of heat flux ($\mathrm{W\,m^{-2}}$) and plume w_p ($\mathrm{cm\,s^{-1}}$) for July 2017 at the model grid cell located 2° S, 140° W in the Equatorial Pacific, where vertical gray patches correspond to period of negative heat flux. 24 h profiles of **(b)** w_p, **(c)** a_p, **(d)** $\rho_\mathrm{p} - \rho$, **(e)** $T_\mathrm{p} - T$ and **(f)** $S_\mathrm{p} - S$ for 13 July 2017.

recurrent nature of the diurnal convection and its variability from one night to another. Each night, convective plumes with w_p reaching up to $3.4\,\mathrm{cm\,s^{-1}}$ develop under surface buoyancy losses (~ -100 to $-200\,\mathrm{W\,m^{-2}}$), extending to depths between 50 and 100 m. The plumes exhibit a distinct asymmetry characterized by a prolonged deepening phase. For instance, on 12 July 2017, convection initiated around 8 p.m. with a shallow (< 10 m, Fig. 3b–f) and weak plume ($\sim 0.3\,\mathrm{cm\,s^{-1}}$, Fig. 3b). As the night progresses, the plume deepens (to ~ 90 m) and intensifies (to $\sim 3\,\mathrm{cm\,s^{-1}}$) for about 12 h, peaking at 08:00 local time (Fig. 3b). Following the gradual transition of the surface heat flux from negative to positive values, the plume weakens and eventually stops at noon. Due to localized instabilities along the density gradient, the mass-flux component can occasionally be activated at depths, as observed on 18 July 2017 at ~ 90 m depth (Fig. 3a). In this case, convection remains weak ($w_\mathrm{p} < 0.5\,\mathrm{cm\,s^{-1}}$) and confined to the neighboring grid cell. This behavior, here due to a local instability, indicates that the EDMF scheme is potentially capable of representing segmented convection not connected to the surface.

Third, the modelled hourly temperatures at 2° S, 140° W are compared to temperature observations available from the TAO mooring at the same location for the period Febru-

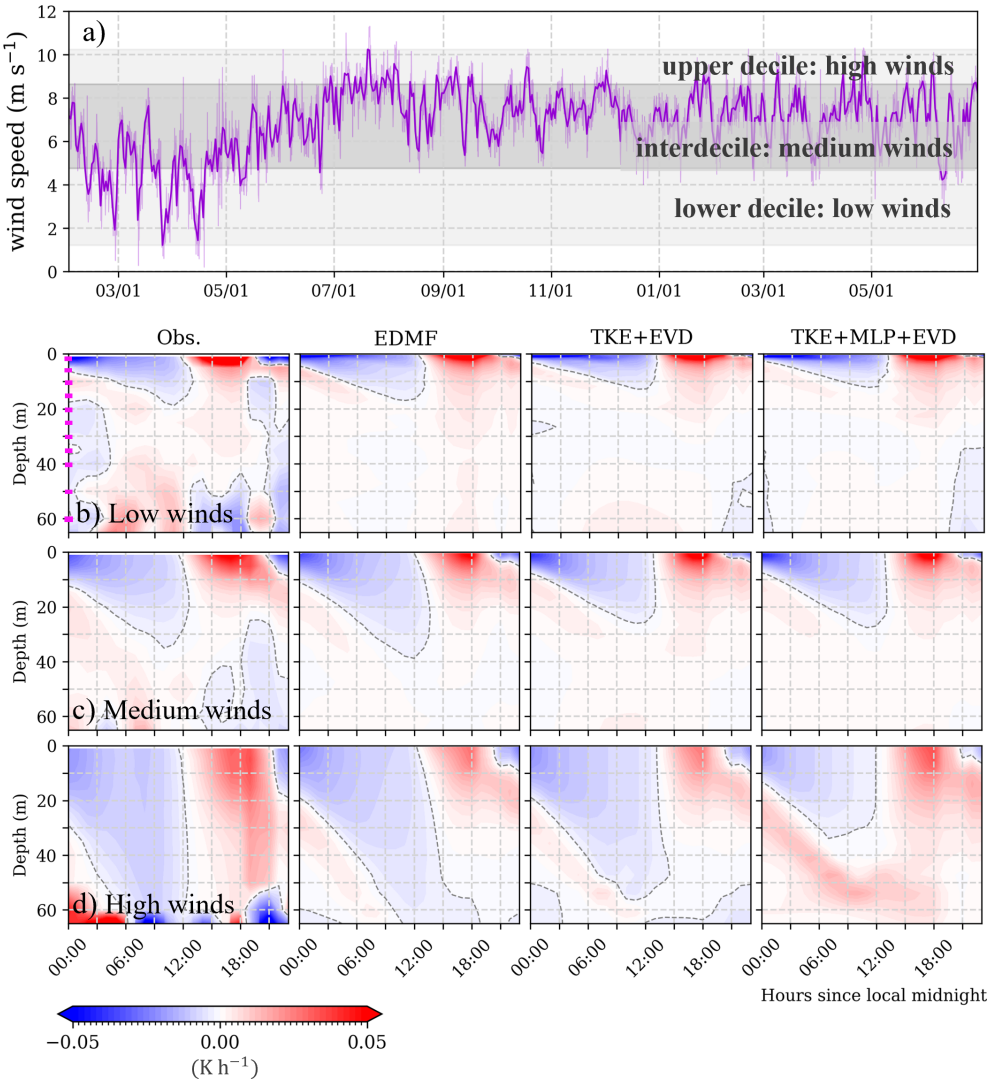


Figure 4. **(a)** Wind speed at location 2° S, 140° W from February 2017 to June 2018, shown at an hourly (light purple) and at a daily resolution (dark purple). **(b–d)** Diurnal composites of the temporal gradient of temperature K h^{-1} for observations (first column), the EDMF simulation (second column), the TKE + EDMF simulation (third column), and the TKE + MLP + EVD simulation (fourth column), categorized by wind speed regimes: **(b)** lower decile (1.22–4.76 m s^{-1}), **(c)** interdecile range (4.77–8.63 m s^{-1}), and **(d)** upper decile (8.64–10.25 m s^{-1}). Magenta squares in panel **(b)** indicate the depths of available in-situ observations.

ary 2017 to June 2018 (515 d), during which enhanced vertical resolution of temperature measurements are available (see Sect. 2.3). The availibility of such observational dataset provides a much more direct and detailed constraint on the temporal diurnal evolution of the upper-ocean temperature. The data are sorted according to the observed daily mean wind speed (Fig. 4a). Days falling within the lowest 10 % (lower decile) of wind speeds are classified as "low wind" conditions, while those in the highest 10 % (higher decile) are classified as "high wind" conditions. The remaining 80 % (interdecile) are classified as "medium wind" conditions. For each wind category, we construct daily composites of the temporal temperature gradient (K h^{-1}). For the period considered, observed cold plume penetration depths increase with wind intensity, from approximately 20 m under low wind conditions to ∼ 60 m under high wind conditions, consistent with the findings of Masich et al. (2021) (Fig. 4b–d). This deepening is reproduced by all three simulations, with EDMF simulation providing the best agreement with the observed cold plume penetration depths. In contrast, the TKE + EVD and TKE + MLP + EVD simulations tend to underestimate these depths by ∼ 10 to 20 m. Additionally, the shape of the cold plumes in the EDMF simulation closely matches observations: cold anomalies continue to propagate for about 1 h after the end of surface cooling, showing that the convective adjustment of water masses is not instanta-

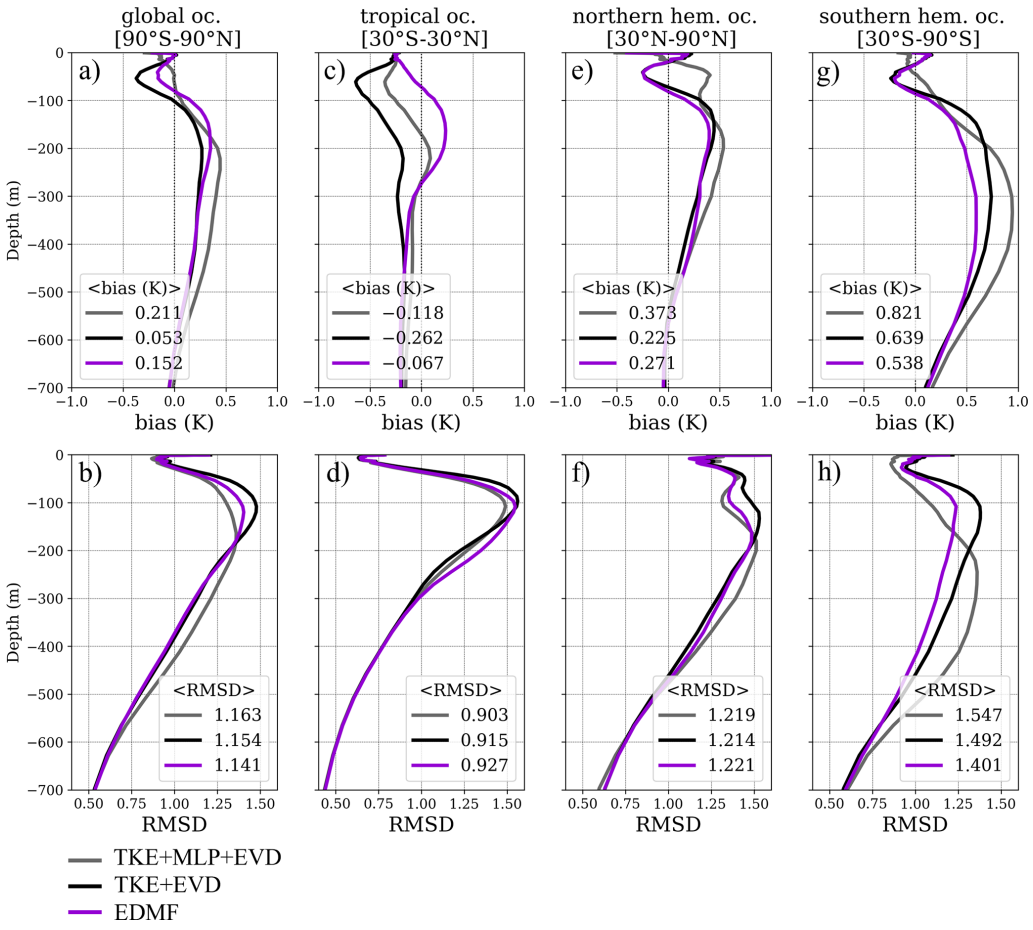


Figure 5. 0–700 m depth profiles of temperature bias (difference between the simulation and the observation; top row) and corresponding RMSD (bottom row) for the three simulations, averaged over the 2005–2020 period for the global ocean **(a, b)**, for the tropical ocean **(c, d)**, for the Northern Hemisphere ocean **(e, f)** and for the Southern Hemisphere ocean **(g, h)**. 0–700 m depth-averaged values of bias and RMSD are provided for each profile in the corresponding legend box.

neous but spreads over a time scale proportional to w_p/h where h is the depth of the unstable water column. In contrast, in the TKE + EVD and TKE + MLP + EVD simulations, cold anomalies cease at depth synchronously with the end of surface cooling. These results highlight the improved representation of shallow diurnal convection processes as a penetrative process by the EDMF parameterization in tropical regions. It should be noted that ad-hoc MLP and EVD modifications aimed at improving the TKE parameterization are now replaced by more physically based processes in EDMF. The composites of the observations exhibit alternating patterns of positive and negative temperature anomalies below the plumes (Fig. 4c), potentially indicative of explicit tides that the simulations do not represent.

3.2 Global temperature patterns

This section focuses on the temperature of upper ocean layer (0–700 m), which accounts for approximately 60 % of ocean heat uptake over the period 1970–2010 (Cheng et al., 2016) and contains the majority of observational data. Complementary analyses over the full 0–2000 m depth range, and for the salinity, are provided in the Supporting Information.

Figure 5 presents globally and regionally averaged temperature bias to temperature observations and root mean square deviation (RMSD) profiles in the upper ocean (0–700 m) for the three simulations. Additionally, Fig. 6a–d shows annual averages of depth-averaged (0–700 m) temperature biases over the simulation period for each ocean basin. At the global scale, the EDMF simulation displays lower 0–700 m depth-averaged temperature bias and RMSD compared to the TKE + MLP + EVD simulation, with averaged values over the simulation period of 0.152 and 0.211 K, respectively, corresponding to a global bias reduction of ~ 30 % (Figs. 5a, b and 6a). Although the TKE + EVD simulation achieves the smallest global depth-averaged bias (0.05 K; Figs. 5a and 6a), this results from the compensation of a cold bias in the upper 0–100 m with a warm bias at greater depths (Fig. 5a). A similar compensation is also present in the EDMF sim-

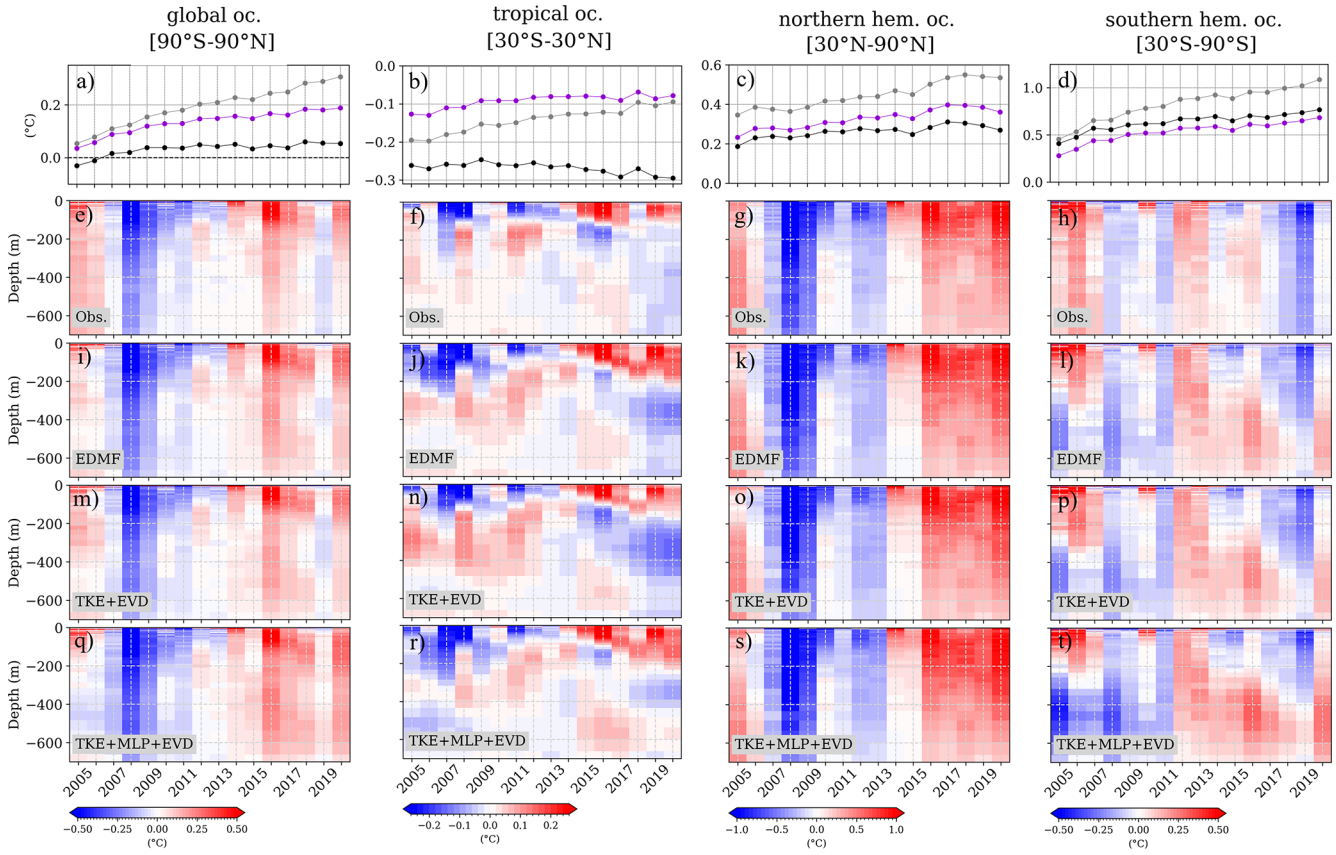


Figure 6. Observed and modelled annually-averaged temperature anomalies (K) from 0–700 m depth, computed relative to the 2005–2020 mean, for (first column) the global ocean, (second column) the tropical ocean, (third column) the Northern Hemisphere ocean, and (fourth column) the Southern Hemisphere ocean. Panels **(a–d)** show the depth-averaged (0–700 m) temperature bias to observations time series for each region.

ulation, but the cold bias in the upper 0–100 m is less pronounced than in the TKE + EVD simulation (Fig. 5a). Considering the 0–2000 m depth range, all three simulations present similar global biases below 700 m (Fig. S2a in the Supplement).

Across all three ocean basins considered, the EDMF simulation consistently produced the lowest depth-averaged bias compared to TKE + MLP + EVD simulation (Figs. 5b, e, g, 6b–d and S2). In the tropical ocean, TKE + EVD and TKE + MLP + EVD present similar cold bias structures, though the addition of the MLP parameterization reduces the upper 300 m cold bias by $\sim$0.25 K in TKE + MLP + EVD (Fig. 5c), leading to a progressive cold bias reduction over time (Fig. 6b). A cold bias peak is observed at $\sim$50 m for both TKE + EVD and TKE + MLP + EVD simulations. In contrast, the EDMF simulation exhibits distinct bias structures, transitioning from a surface cold bias to a warm bias between 100 and 200 m depth (Fig. 5c), which also contributes to a decrease of the tropical cold bias over time (Fig. 6b). This highlights the effect of a better physical representation the diurnal plumes in EDMF, which transport warm upper-ocean water downwards.

In both the northern and southern oceans, TKE + EVD and EDMF simulations exhibit similar vertical bias structures, characterized by alternating warm-cold-warm anomalies with increasing depth (Fig. 5e and g). In contrast, the TKE + MLP + EVD simulation displays a predominantly warm bias throughout the water column (Fig. 5e and g), resulting in higher depth-averaged warm biases over time (Fig. 6c and d). In the 150–700 m depth range of the southern ocean, both TKE + EVD and EDMF simulations substantially reduce the warm bias observed in TKE + MLP + EVD, with EDMF achieving the largest reduction (up to 0.4 K, Fig. 5g) and the lowest depth-averaged warm biases over time (Fig. 6d).

The global interannual variability of observed upper-ocean temperature anomalies (relative to the 2005–2020 mean), characterized by a cooling phase during 2007–2011 followed by a warming phase from 2014 onward, is reproduced by all three simulations, although some discrepancies between the simulations exist (Fig. 6e, i, m, and q). For example, the simulations underestimate the global warm anomalies observed throughout the water column in 2005–2006 (Fig. 6i, m, and q). The underestimation is most pronounced

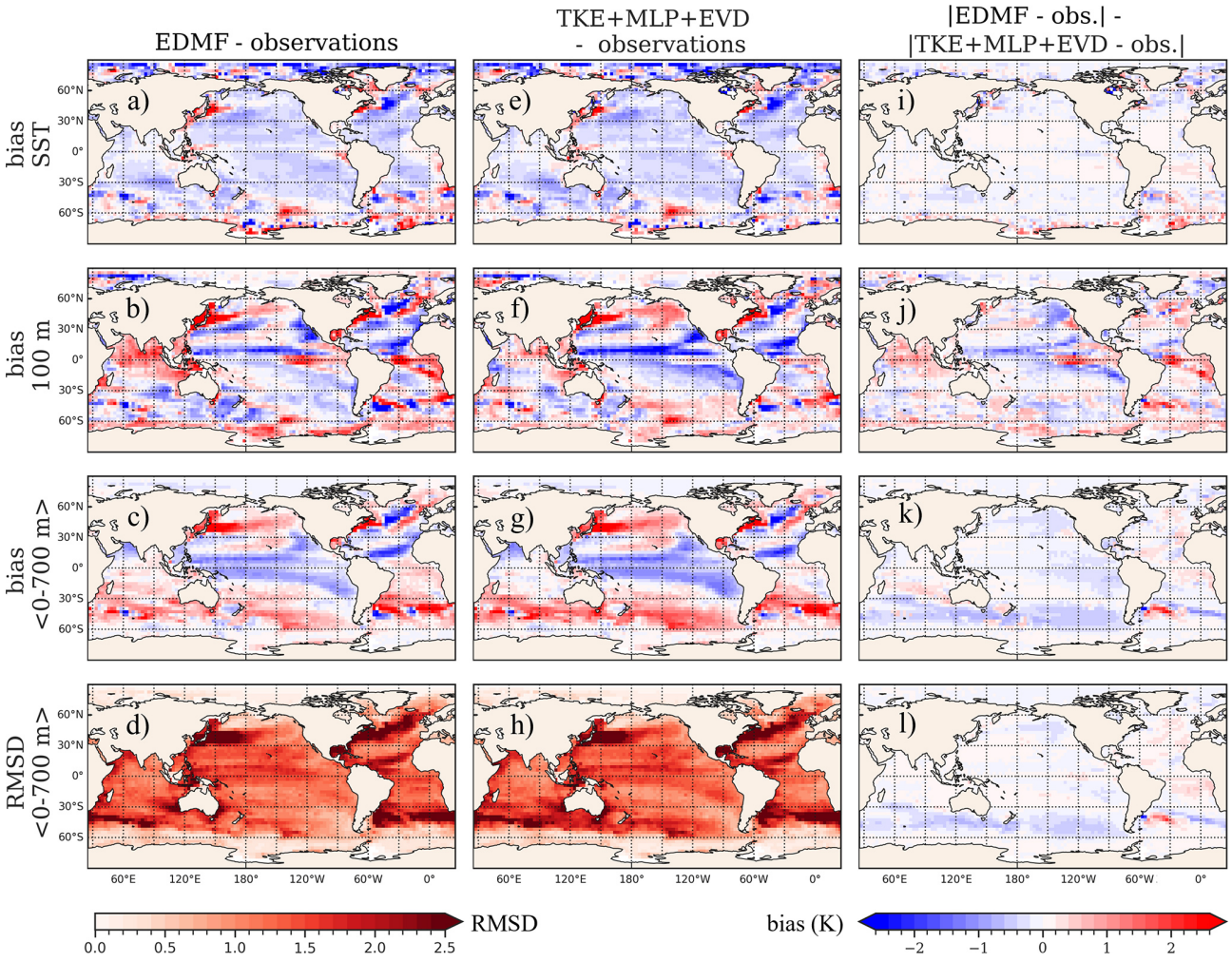


Figure 7. (a–d) Maps of bias between the EDMF simulation and the observations for SST (first row), temperature at 100 m (second row), 0–700 m depth-averaged temperature between (third row) and the corresponding 0–700 m averaged RMSD (fourth line). **(e–h)** Same as **(a–d)** but for the TKE + MLP + EVD simulation. **(i–k)** Maps of absolute differences between the biases for the three depth ranges considered, and **(l)** the corresponding RMSD differences.

in the TKE + MLP + EVD simulation, which produces cold anomalies between 200 and 600 m depth (Fig. 6q). This bias primarily originates in the Southern Hemisphere ocean, where all three simulations show cold anomalies in this depth range in 2005–2006, that are not supported by observations; the TKE + MLP + EVD simulation exhibits the strongest colder anomalies (Fig. 6h, l, p, and t). In the tropical ocean, all simulations overestimate the warm anomalies observed from 2005 to 2012 between ∼ 200 to ∼ 500 m depth, with TKE + EVD exhibiting warmest anomalies (Fig. 6f, j, n, and r). From 2018 onward, the TKE + MLP + EVD fails at representing the observed vertical extent of the cold anomalies, which spread from ∼ 100 to 700 m depth (Fig. 6f and r), while EDMF best represents these cold anomalies in terms of both depths and intensities (Fig. 6f and j).

The performance of the EDMF and TKE + MLP + EVD simulations in representing the 0–700 m temperature fields averaged over the simulation period is further analyzed in Fig. 7. Complementary results for the 700–2000 m depth range are provided in Fig. S4 in the Supplement, and for TKE + EVD simulation in Fig. S5 in the Supplement. Both simulations exhibit similar large-scale patterns of temperature bias in the 0–700 depth layer, characterized by cold anomalies across the tropical oceans and warm anomalies at high latitudes (Fig. 7c and g). Compared to TKE + MLP + EVD, the EDMF simulation generally reduces the 0–700 m temperature bias by ∼ 0.5–1 K on a basin-wide scale, except in the tropical Atlantic and Indian Oceans, where EDMF shows slightly warmer anomalies (∼ 0.2 K) than TKE + MLP + EVD (Fig. 7k). As expected from Fig. 5, the influence of the mixing parameterization is limited at the surface and becomes more pronounced at depths (Fig. 7a, e, b, and f). At the surface, sea surface temperature (SST) bias fields are similar between the two simulations, character-

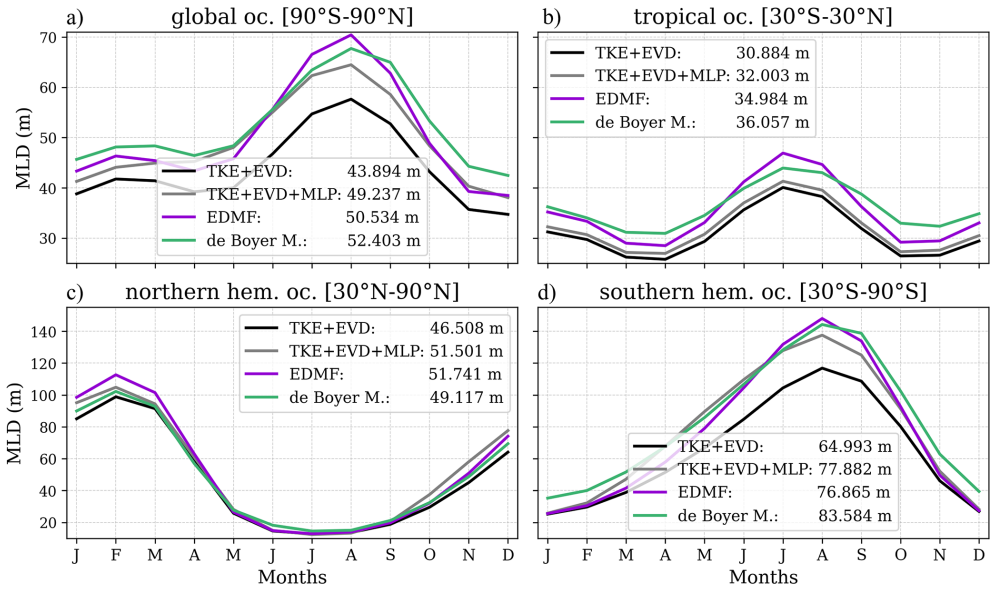


Figure 8. Seasonal cycle of MLD (in m) from the three simulations and the de Boyer Montégut (2024) dataset in the global **(a)**, tropical **(b)**, Northern Hemisphere **(c)** and Southern Hemisphere **(d)** ocean. Mean MLD values for each dataset are indicated within each panel.

ized by widespread cold anomalies across much of the global ocean (Fig. 7a and e). Exceptions include the western boundary current regions (Gulf Stream and Kuroshio), equatorial upwelling zones off Peru and Benguela, and the southern Pacific Ocean, where both simulations show warm biases. These regional SST warm biases are consistent with known biases in the forcing products, particularly due to a misrepresentation of longwave and shortwave fluxes (Zhang et al., 2023). Furthermore, western boundary currents are strongly affected by horizontal processes, including mesoscale eddies, fronts, and lateral advection, which are not fully resolved at the $1/4°$ horizontal resolution of our simulations. Consequently, these warm anomalies do not necessarily indicate a deficiency of the vertical mixing schemes, as they may partly reflect errors in the representation of horizontal dynamics and air–sea interactions.

At 100-m depth, the temperature bias fields of the two simulations (Fig. 7b and f) resemble those of the 0–700 m depth layer (Fig. 7c and g), although regional discrepancies emerge. For instance, the EDMF simulation exhibits a warmer bias of up to 1.5 K compared to TKE + MLP + EVD in the equatorial upwelling zones (Fig. 7b, f, and j). This may result from the downward transport of warm surface waters by nighttime convection, which partly counteracts the cooling effect associated with upwelling. Conversely, TKE + MLP + EVD exhibits colder anomalies by ~ 1 K in most of the tropical Pacific. This contrast suggests that the diurnal convection represented by EDMF contributes to reducing the tropical Pacific cold bias by transporting and mixing warm upper-ocean waters downward. Overall, these results indicate that the more physically based representation of diurnal convection in EDMF contributes to a reduction of the tropical Pacific cold bias.

In the 700–2000 m depth layer, the patterns and intensities of the temperature bias and corresponding RMSD are similar between the two simulations, with basin-wide bias differences below 0.4 K (Fig. S4). This result highlights the limited influence of the OBL parameterization in this depth range, where modifications to the temperature pattern occur over much longer timescales.

The tropical cold biases in the 0–700 m depth layer are more pronounced in the TKE + EVD simulation (Fig. S5g) compared to both EDMF and TKE + MLP + EVD simulations (Fig. 7c and g). This confirms that the EVD scheme alone is less effective at reproducing temperature values in this region (Fig. S5k), highlighting the potential benefit of an additional source of TKE in the mixed-layer through the MLP parameterization. The enhanced cold anomalies in TKE + EVD extend towards the mid-latitudes of the southern ocean (20–40° S), which compensate for the warm biases observed in the two other simulations in this region (Fig. S5f, g, j, and k; Fig. 7). Interestingly, opposite patterns are observed in the high latitudes where the warm biases at depths are enhanced in TKE + EVD (Fig. S5f) compared to EDMF and TKE + MLP + EVD simulations (Fig. 7b and f). In this case again, the EVD scheme alone fails at representing the observed temperature patterns.

3.3 Mixed-layer depth (MLD)

The global modeled seasonal cycle of MLD from both the EDMF and TKE + MLP + EVD simulations is close to the observed MLD throughout the year, although it is slightly

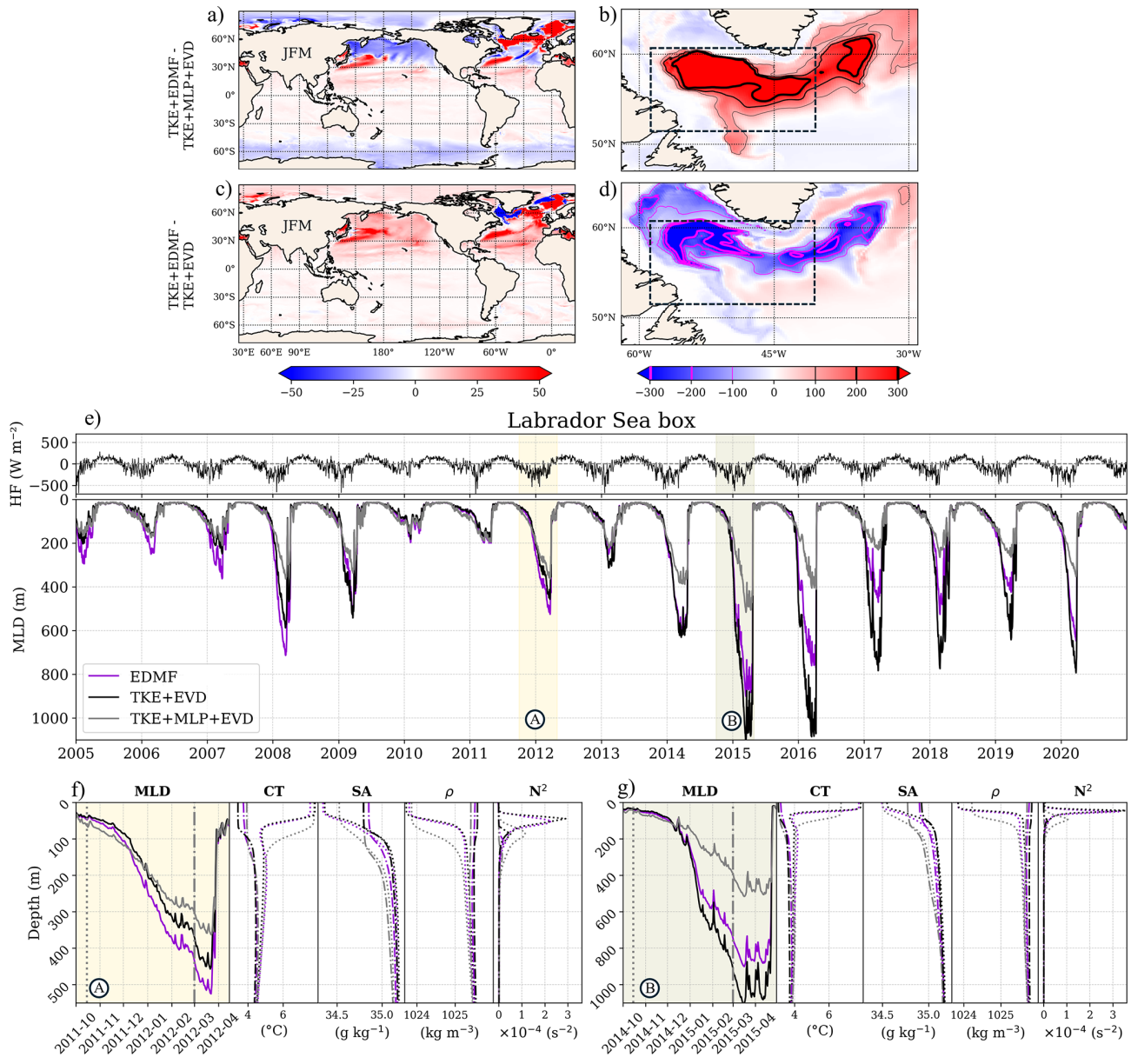


Figure 9. **(a–d)** Maps of mixed layer depth (MLD) differences (in m) computed for the JFM period between the EDMF simulation and **(a, b)** the TKE + MLP + EVD, and **(c, d)** the TKE + EVD simulations. **(e)** Time series of surface heat flux ($\mathrm{W\,m^{-2}}$) and MLD (m) for the three simulations, averaged over the dashed black box representing the Labrador Sea shown in **(b, d)**. **(f)** MLDs during period A, along with vertical profiles of conservative temperature (CT, °C), absolute salinity (SA, $\mathrm{g\,kg^{-1}}$), density (ρ, $\mathrm{kg\,m^{-3}}$) and N^2 ($\mathrm{s^{-2}}$) for selected days prior to (dotted lines) and during (dashed-dotted lines) the deep convection period, shown for all three simulations. **(g)** Same as **(f)** but for period B.

deeper by ∼ 5 m during JJAS and shallower by ∼ 5 m during the rest of the year (Fig. 8a). In the tropical ocean, the EDMF simulation produces a seasonal MLD cycle that is closest to observations, while the other two simulations underestimate the observed cycles throughout the year (Fig. 8b). In both the northern and Southern Hemisphere oceans, all simulations underestimate the observed monthly MLD during boreal and austral summers, respectively (Fig. 8c and d). During winter periods, the EDMF simulation produces deeper MLDs than the two EVD simulations in both extratropical oceans (Fig. 8c and d). This results in deeper-than-observed MLDs in the Northern Hemisphere ocean (Fig. 8c), while EDMF MLD is in close alignment with the observations in the Southern Hemisphere ocean (Fig. 8d).

The deeper monthly MLDs observed for EDMF in the Northern Hemisphere ocean originate from the deep con-

vective regions of the Northern Atlantic ocean (Labrador, Irminger and Norwegian Sea), where MLDs from EDMF exceed those of TKE + MLP + EVD by up to 300 m during the January–February–March (JFM) period (Fig. 9a, b, and e). In the rest of the Northern Hemisphere ocean, the MLDs from TKE + MLP + EVD are ∼ 30 m deeper than those from EDMF (Fig. 9a). An opposite pattern is observed when comparing EDMF and TKE + EVD simulations during JFM (Fig. 9c–e). In most of the Northern Hemisphere ocean, EDMF produces MLDs that are ∼ 20 to 50 m deeper than those from TKE + EVD (Fig. 9c). However, in the Labrador Sea, TKE + EVD generates JFM-averaged MLDs from 100 to 300 m deeper than those produced by EDMF (Fig. 9d and e).

To explain the discrepancies in MLDs among the simulations in the Labrador Sea, we investigate the temperature, salinity, density and Brunt–Väisälä frequency (N^2) profiles from the three simulations, both prior to and during the deep convection periods in winters 2011–2012 and 2014–2015 (Fig. 9f). Before the onset of the deep convection period, the TKE + MLP + EVD simulation exhibits deeper and weaker density gradients than those found in the TKE + EVD simulation, resulting in deeper MLDs in TKE + MLP + EVD by several tenth of meters. Correspondingly, the stratification levels in TKE + MLP + EVD, as indicated by N^2 values ($\sim 1 \times 10^{-4}\,\mathrm{s}^{-2}$), are lower than those in TKE + EVD ($> 2.5 \times 10^{-4}\,\mathrm{s}^{-2}$). This difference arises from the MLP parameterization, which enhances mixing in the thermocline year-round, especially at high latitudes (see Sect. 2.1). The enhanced mixing erodes the vertical temperature gradients, thereby reducing the potential energy barrier that resists overturning. Consequently, one would expect the weaker preconditioning stratification in TKE + MLP + EVD to favor deeper convection and MLDs than in TKE + EVD during the buoyancy loss period. However, the opposite occurs: the MLP parameterization suppresses residual instabilities within the mixed layer. This reduces the occurrence of conditions triggering the EVD scheme and consequently decreases the frequency of EVD activations. The reduced EVD activity limits further deepening of the mixed layer, resulting in shallower MLDs by up to ∼ 150 and ∼ 600 m in TKE + MLP + EVD compared to TKE + EVD in winter 2011–2012 and 2014–2015, respectively. This highlights the regulation of the mixing by EVD through the MLP parameterization.

The stratification depths and intensities prior to the onset of the deep convection are similar between EDMF and TKE + EVD simulations (Fig. 9f and g), but the MLDs during the convection period differ between the two. In 2014–2015 before the convection period, the water column is highly stratified for both EDMF and TKE + EVD ($N^2 > 3 \times 10^{-4}\,\mathrm{s}^{-2}$). Under intense surface buoyancy loss, the large mixing coefficient values assigned in TKE + EVD simulation is more efficient to erode the thermocline stratification than the convective velocities in EDMF simulation, resulting in shallower MLDs by ∼ 200 in EDMF simulation.

With mild stratification conditions for both EDMF and TKE + EVD simulations ($2.2 < N^2 < 2.8 \times 10^{-4}\,\mathrm{s}^{-2}$) in the preconditioning period of 2011–2012, the mixing coefficient values assigned in TKE + EVD produced MLDs that are ∼ 50 m shallower than those of EDMF, because of limited residual instabilities and thus limited occurrences of EVD activations. This result is consistent with weaker surface buoyancy loss in 2011–2012 than in 2014–2015 (Fig. 9e).

Note that, although individual Argo-based MLD estimates are available for the Labrador Sea (e.g., Holte et al., 2017), a direct comparison with the box-averaged MLD shown here would require accounting for the heterogeneous spatial and temporal sampling of Argo profiles and applying consistent MLD diagnostics to the model profiles. Such a model-observation comparison is beyond the scope of the present study.

4 Surface heat fluxes adjustments to EDMF

The choice of vertical mixing parameterization modifies the SST. These SST differences can in turn modify the surface heat-fluxes. In this section, we quantify how the use of the mass-flux relative to EVD, affects the surface heat flux budget and identify the processes responsible for these adjustments. For that we compare only the EDMF simulation with the TKE + EVD simulation (TKE + EVD + MLP is not considered here).

4.1 Surface heat flux budget

The subsequent analysis is carried out for the climatological seasons of JFM (January–February–March) and JAS (July–August–September) over several oceanic regions, for both the EDMF and TKE + EVD simulations.

At the global scale, assuming negligible contributions from external freshwater and other non-surface heat sources, the change in total ocean heat content between the two simulations ($\Delta\delta T(t)$) is only determined by the net surface heat flux (SURF) induced by the change in vertical scheme:

$$\Delta\delta T(t) = \delta T_{\mathrm{EDMF}}(t) - \delta T_{\mathrm{TKE+EVD}}(t) = \mathrm{SURF}, \tag{10}$$

and the components of SURF expressed as:

$$\begin{aligned}
&\Delta \mathrm{SW}_{\mathrm{net}} = \mathrm{SW}_{\mathrm{net\ EDMF}}(z=0,t)\mathrm{SW}_{\mathrm{net\ TKE+EVD}}(z=0,t),\\
&\Delta \mathrm{LW}_{\uparrow} = \mathrm{LW}_{\uparrow \mathrm{EDMF}}(z=0,t) - \mathrm{LW}_{\uparrow\ \mathrm{TKE+EVD}}(z=0,t),\\
&\Delta \mathrm{SH} = \mathrm{SH}_{\mathrm{EDMF}}(z=0,t) - \mathrm{SH}_{\mathrm{TKE+EVD}}(z=0,t) \text{ and}\\
&\Delta \mathrm{LH} = \mathrm{LH}_{\mathrm{EDMF}}(z=0,t) - \mathrm{LH}_{\mathrm{TKE+EVD}}(z=0,t),
\end{aligned} \tag{11}$$

with $\mathrm{SW}_{\mathrm{net}}$ the net shortwave radiation flux, $\mathrm{LW}_{\mathrm{net}}$ the net longwave radiation flux, SH the sensible heat flux and LH the latent heat flux. The ↓ and ↑ correspond to downward and upward, respectively.

This leads to changes in the simulated global mean temperature (in K) defined as:

$$\delta T(t) = T(t) - T(0) = Q_{\text{net}}(z=0,t), \text{ with} \quad (12)$$

$$Q_{\text{net}}(z=0,t) = \sum_{i=1}^{t} \frac{Q_{\text{net}}(i) A_z \Delta t}{V \rho_0 C_p} \text{ with}$$

$$A_z = e_1(x,y) e_2(x,y) t_{\text{mask}}(x,y,z), \text{ and} \quad (13)$$

$$T(t) = \sum_{z=0}^{z=h} \frac{T(z,t) V z}{V} \text{ with } V_z = A_z e_3(x,y,z), \quad (14)$$

where Q_{net} is the net downward air–sea heat flux ($\mathrm{W\,m^{-2}}$), e_1 and e_2 are the horizontal grid-cell dimensions, e_3 is the grid-cell thickness, t_{mask} is the mask used to select the ocean grid cells belonging to the region considered, V is the total ocean volume (in $\mathrm{m^3}$), ρ_0 is the density of seawater at the surface ($\mathrm{kg\,m^{-3}}$), C_p is the specific heat capacity of seawater ($\mathrm{J\,kg^{-1}\,K^{-1}}$), Δt the elapsed time (in s), T the temperature (K), and h is the bottom vertical level. This means that $\delta T(t)$ is controlled solely by the net surface heat forcing at global scale.

The air–sea heat flux (Q_{net}) is decomposed as:

$$Q_{\text{net}} = \text{SW}_{\text{net}} + \text{LW}_{\text{net}} + \text{SH} + \text{LH}, \quad (15)$$

$$\text{where } \text{SW}_{\text{net}} = \text{SW}_{\downarrow} - \text{SW}_{\uparrow} \text{ and}$$

$$\text{LW}_{\text{net}} = \text{LW}_{\downarrow} - \text{LW}_{\uparrow}. \quad (16)$$

The bulk formulae of the ocean model provide SH and LH. The downward longwave flux $\text{LW}_{\downarrow}$ and $\text{SW}_{\downarrow}$ are prescribed from the ERA5 reanalysis and are common to the two simulations, while the $\text{LW}_{\uparrow}$ and $\text{SW}_{\uparrow}$ are diagnosed for each simulation from Eq. (14).

4.2 Seasonal and regional adjustments

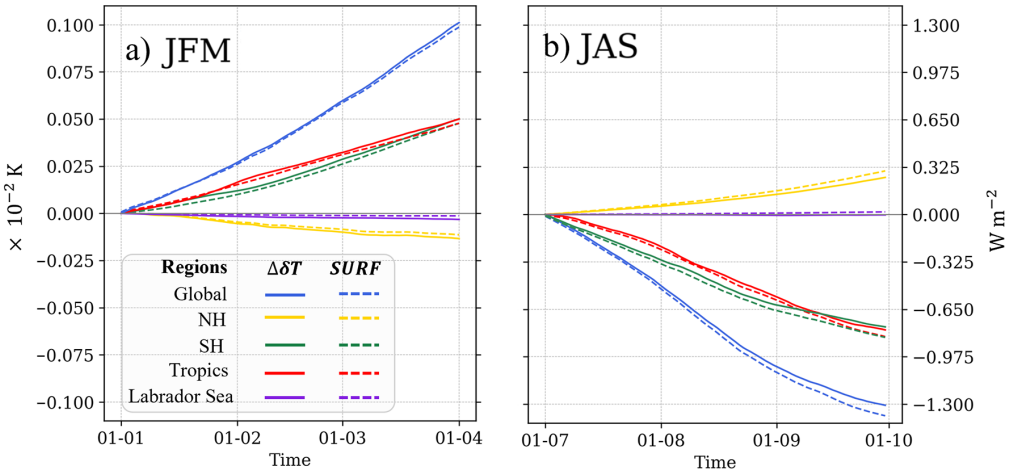
The $\Delta\delta T(t)$ and SURF time series (Fig. 10a and b) show high consistency at global and seasonal scales. At the end of the period, the cumulative surface fluxes do not deviate by more than 3 % from the temperature variations, which indicate a good closure of the global heat budget.

In the global ocean, the $\Delta\delta T(t)$ and SURF timeseries exhibit opposite behaviors between the JFM and JAS seasons, with increasing positive values in JFM and decreasing negative values in JAS (Fig. 10a and b). Positive SURF values indicate that the net surface heat loss in EDMF simulation is less than in TKE + EVD simulation. The higher component of SURF in EDMF arises primarily ($\sim 59\,\%$) from reduced latent heat (LH) loss and secondarily ($\sim 27\,\%$) from reduced sensible heat (SH) loss relative to TKE + EVD (Fig. 10c). Because heat fluxes are defined as positive downwards, positive ΔLH and ΔSH, correspond to weaker upward (negative) LH_{EDMF} and SH_{EDMF} compared to $\text{LH}_{\text{TKE+EVD}}$ and $\text{SH}_{\text{TKE+EVD}}$. These reduced LH_{EDMF} and SH_{EDMF} values result from globally cooler SSTs in EDMF ($T_{\text{air}} - \text{SST} > 0$), which reduces the air–sea temperature and humidity gradients and thus the turbulent heat loss to the atmosphere. The longwave upward radiative flux differences ($\Delta\text{LW}_{\uparrow}$) contribution to SURF is more moderate ($\sim 10\,\%$), reflecting slightly weaker infrared cooling in EDMF due to cooler SST. Shortwave fluxes differences (ΔSW) contribute only marginally to SURF ($\sim 2\,\%$) and originate from differences in $\text{SW}_{\uparrow}$, which are linked to regional differences in sea-ice concentration – most notably along the Greenland margins and in the Sea of Okhotsk (Sect. S2 in the Supplement; Fig. S7e and f in the Supplement). Similar contributions of ΔLH, ΔSH and $\Delta\text{LW}_{\uparrow}$ are found in the Southern Hemisphere and tropical oceans (Fig. 10c).

In the Northern Hemisphere ocean, the negative SURF values in JFM are again dominated by contributions from ΔLH, followed by ΔSH and $\Delta\text{LW}_{\uparrow}$ (Fig. 10a and c). Here, negative values indicate stronger upward LH_{EDMF}, SH_{EDMF} and $\text{LW}_{\uparrow\text{EDMF}}$ relative to EVD. These enhanced turbulent and radiative losses arise from warmer SSTs in EDMF due to less turbulent entrainment at the mixed-layer base, which increase the air–sea temperature and humidity gradient and thus enhance heat loss to the atmosphere. The Labrador Sea also exhibits negative SURF values in JFM – consistent with SURF in the Northern Hemisphere – but with comparable contributions from ΔLH and ΔSH (Fig. 10a and c). In this region, extremely cold and dry winter conditions produce low near-surface humidit (q_{a}), while higher SSTs lead to higher specific humidity saturation ($q_{\text{sat}}(\text{SST})$) in the EDMF simulation in accordance with the Clausius–Clapeyron relation. The SST adjustment and the Clausius–Clapeyron law control the turbulent heat flux sensitivity between the two simulations.

As expected from the seasonal transition, opposite patterns emerge during JAS, with negative SURF values in the global, Southern Hemisphere, and tropical oceans, and positive SURF values in the Northern Hemisphere ocean and Labrador Sea (Fig. 10b and d). This result stems from the fact that turbulent entrainment is more intense with EVD than with EDMF in JAS, i.e., during winter in the Southern Hemisphere ocean, whereas it is the opposite in the Northern Hemisphere ocean, where the vertical mixing is more intense in summer with EDMF than with EVD. As in JFM, ΔLH remains the dominant contributor to SURF, followed by ΔSH and $\Delta\text{LW}_{\uparrow}$. An exception occurs again in the Labrador Sea where contributions of ΔLH and ΔSH are of similar magnitude.

The opposite adjustments of SURF and its individual components observed during the JAS season (Fig. 10b) are driven by positive SST anomalies induced by the EDMF scheme. These adjustments occur with proportions comparable to those diagnosed during the JFM season. At the global scale, the SURF signal is controlled by the Southern Hemisphere and the tropical oceans rather than by the Northern Hemisphere ocean, for both seasons. This reflects the larger oceanic surface area in the Southern Hemisphere, which dominates the global heat budget.



× 10^{-2} K
$W\ m^{-2}$

c) JFM

	$\Delta(T_{air} - SST)$	$SURF$	ΔSW	$\Delta LW_{\uparrow}$	ΔLH	ΔSH
Global	3.57 *46.4*	3.82 *49.7*	-0.09 *-1.17*	0.45 *5.85*	2.38 *30.9*	1.09 *14.17*
NH	-0.26 *-3.38*	-0.12 *-1.56*	0.02 *0.26*	-0.02 *-0.26*	-0.06 *-0.78*	-0.05 *-0.65*
SH	2.38 *29.6*	1.84 *23.9*	-0.11 *-1.43*	0.26 *3.38*	1.00 *13.0*	0.68 *8.84*
Tropics	1.45 *18.9*	2.10 *27.3*	0.00 *0.00*	0.21 *2.73*	1.44 *18.7*	0.45 *5.85*
Labrador Sea	-0.03 *-0.39*	-0.07 *-0.91*	-0.00 *-0.00*	-0.01 *-0.13*	-0.03 *-0.39*	-0.03 *-0.39*

d) JAS

× 10^{-2} K
$W\ m^{-2}$

Global	-4.18 *-54.3*	-4.97 *-64.6*	0.01 *0.13*	-0.58 *-7.54*	-2.80 *-36.4*	-1.60 *-20.8*
NH	1.12 *14.6*	0.87 *11.3*	-0.03 *-0.39*	0.14 *1.82*	0.50 *6.50*	0.25 *3.25*
SH	-2.65 *-34.5*	-2.95 *-38.4*	0.03 *0.39*	-0.34 *-4.42*	-1.44 *-18.7*	-1.21 *-15.7*
Tropics	-2.64 *-34.3*	-2.89 *-37.6*	0.00 *0.00*	-0.37 *-4.81*	-1.87 *-24.3*	-0.65 *-8.45*
Labrador Sea	0.08 *1.04*	0.05 *0.65*	-0.00 *-0.00*	0.01 *0.13*	0.02 *0.26*	0.02 *0.26*

$\Delta(T_{air} - SST) = (T_{air} - SST_{EDMF}) - (T_{air} - SST_{TKE+EVD})$
$SURF = Q_{net\ EDMF}(z = 0, t) - Q_{net\ TKE+EVD}(z = 0, t)$
$\Delta SW = SW_{net\ EDMF} - SW_{net\ TKE+EVD}$
$\Delta LW_{\uparrow} = LW_{\uparrow\ EDMF} - LW_{\uparrow TKE+EVD}$
$\Delta LH = LH_{EDMF} - LH_{TKE+EVD}$
$\Delta SH = SH_{EDMF} - SH_{TKE+EVD}$

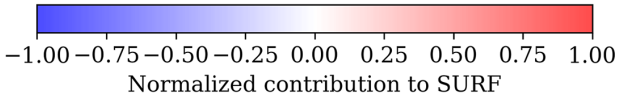


Figure 10. Time series of SURF (10^{-2} K on the left y-axis; W m^{-2} on the right y-axis) for the climatological seasons of JFM **(a)** and JAS **(b)**, computed for the global, Northern Hemisphere (NH), Southern Hemisphere (SH), tropical oceans and the Labrador Sea. Corresponding cumulative values of SURF, ΔSW, $\Delta LW_{\uparrow}$, ΔLH, ΔSH, expressed in 10^{-2} K and in W m^{-2} (in italics) for JFM **(c)** and JAS **(d)**. The sign convention of these values is given in Eq. (9). The colorbar indicates the normalized contribution of each heat flux component to SURF.

Consequently, the global positive SURF anomalies in JFM (Fig. 10a) are associated with negative SST anomalies, and vice-versa in JAS (Fig. 10b) where negative SURF anomalies are associated with positive SST anomalies. This result indicates that the entrainment at the base of the mixed layer is stronger for EDMF than for TKE + EVD during JFM i.e. in the summer hemisphere, because the seasonal cycle is dominated by the Southern Hemisphere ocean, and vice-versa in JAS. This shows that the mixing process is more enhanced for TKE + EVD than for EDMF in winter and vice-versa in summer.

This global entrainment response, supported by the Southern Hemisphere and the tropical oceans, is partly offset by opposite SURF adjustments in the Northern Hemisphere

ocean and Labrador Sea. In these regions, EDMF induces reduced vertical mixing during JFM and enhanced mixing during JAS, leading to negative and positive SURF anomalies, respectively. However, the contribution of the Northern Hemisphere ocean does not dominate the global signal. This response is consistent with the MLDs shown in Fig. 9e and f, particularly from 2015 onward, where the TKE + EVD simulation exhibits systematically deeper MLDs than EDMF. These deeper MLDs result from very frequent EVD activations, which lead to a significant deepening of the mixed layer.

4.3 Implications for ocean heat uptake

The global temperature adjustment induced by the EDMF scheme results from adjustments in surface heat fluxes, and in decreasing order: ΔLH, ΔSH, $\Delta LW_{\uparrow}$. In terms of energy, this adjustment corresponds to an average amount of energy on the order of $10^7\,\mathrm{J\,m^{-2}}$, estimated from $\Delta J = \rho_0 C_p h (= 2500\,\mathrm{m})\Delta T (= 0.001\,\mathrm{K})$, which represents $1.3\,\mathrm{W\,m^{-2}}$ on a seasonal timescale. This adjustment represents $\sim 6.5\,\%$ of the global net surface heat flux climatology ($\sim 20\,\mathrm{W\,m^{-2}}$) proposed by Tomita et al. (2021). Such non-negligible adjustment suggests that the EDMF parameterization can substantially influence processes associated with water-mass formation such as modal water production, particularly in subpolar or subtropical regions. Consequently, the use of EDMF has the potential to improve physical realism of vertical mixing and surface-interior heat exchange, thereby contributing to more reliable climate simulations.

5 Discussion and Conclusion

This study presents the first global implementation and evaluation of the EDMF parameterization for oceanic convection within the NEMO framework. The EDMF approach has the advantage of describing in a unified way both diffusive (local) and non-diffusive (non-local) turbulent mixing that are the main mixing regimes of the OBL, with numerics tailored to each process (Giordani et al., 2020). By explicitly representing the non-local transport associated with convective plumes, EDMF fundamentally departs from the EVD approach combined with the MLP parametrization that are traditionally used in NEMO, in which convection is represented through strong local diffusion. Our results reveal several key improvements associated with EDMF, in terms of convective regimes, global upper-ocean temperature and MLD compared to a state-of-the-art EVD + MLP approach.

The global configuration allows convective regimes to be assessed under realistic and spatially varying oceanic conditions, including the effects of horizontal advection, over a range of forcing conditions and on interannual timescales. Based on a 16-year simulation period, we show that EDMF successfully captures the two distinct regimes of oceanic convection: shallow diurnal convection prevalent in the tropics, and deep wintertime convection occurring in subpolar regions. In the tropics, EDMF closely reproduces the penetrative and temporally asymmetric behavior of shallow convection, including its persistence beyond the cessation of nighttime surface cooling. In comparison, EVD-based approaches fail to represent this persistence and they underestimated the plume penetration depths. In the northern Atlantic subpolar region, EDMF reproduced the seasonality, depths and intensities of the observed convective plumes. In particular, the scheme captured the major deep convection event of winter 2014–2015 that occurred in the Labrador and Irminger Seas. In comparison, the TKE + EVD + MLP simulation largely underestimated the MLDs during this event. As MLP weakens the stratification during the preconditioning period (autumn), the activations of EVD are less frequent, resulting in weak vertical mixing and shallow MLDs.

At the global scale, EDMF reduces the temperature biases by $\sim 30\,\%$ in the upper 700 m compared to the state-of-the-art TKE + MLP + EVD configuration. This improvement primarily stems from a more realistic representation of convection basin-wide, leading to improved representation of the vertical distribution of heat within the mixed layer and thus reduced warm biases in both hemispheres. In the tropics, the long-standing subsurface cold bias in EVD-based simulations is mitigated in EDMF as the scheme conveys warm waters from the upper-layers downwards. These reductions in temperature biases obtained with EDMF should nevertheless be interpreted with caution as they reflect the combined effect of EDMF, the other parameterizations, the surface forcing and their interactions. Further improvements in the global mean state of temperature may therefore be possible through a joint re-tuning of the model components. These results should thus be viewed as an indication of the potential beneficial impact of EDMF formulation, rather than as a standalone demonstration of improved physical realism.

The EDMF parameterization further modifies the oceanic heat balance by adjusting surface heat fluxes. This adjustment, primarily driven by latent heat flux, changes the net climatological surface heat balance by approximately 6 %–7 %. This has consequences for the worldwide SST diurnal cycle and global subtropical mode waters, which are mainly produced in the Gulf Stream (Gan et al., 2023). In coupled ocean-atmosphere mode, adjustments to large-scale atmospheric circulation, surface fluxes and associated precipitation are also to be expected.

Overall, this global-scale assessment demonstrates the impact of introducing EDMF representation of local and non-local vertical mixing into a global ocean model. This study further illustrates that the EDMF parameterization is a credible alternative to the traditional TKE + EVD + MLP approach, offering a physically grounded alternative for mixed-layer deepening processes. The EDMF formulation removes the need for an additional empirical adjustment such as MLP within the convective mixing scheme, as density instabilities

are directly used to activate the mass-flux formulation regardless of their origin. The overarching objective of EDMF is indeed to move away from the use of empirical adjustments such as EVD and MLP and towards a more physically-based representation of turbulent mixing at the base of the mixed-layer. We recognize that this is a challenging task, given that the NEMO configuration has been originally tuned around the existing EVD and MLP framework. Consequently, future work will include parameters tuning to consider EDMF and other evolving parameterizations jointly rather than tuning each component independently.

For climate simulations, we plan to adjust the EDMF parameters, particularly those controlling lateral exchanges between convective plumes and their environment, using the High-Tune method (Couvreux et al., 2021). High-Tune provides a semi-automatic offline calibration framework based on an ensemble of simulations, offering a more systemic alternative to empirical parameter tuning while helping to avoid over-calibration.

A remaining question is how convection interacts with double-diffusion mixing. This is an important issue, as both processes play key roles in the formation and transformation of water masses and contribute to the large-scale thermohaline circulation (Zhang et al., 1998). Their interaction therefore warrants further investigation.

Data availability. All simulations presented in this paper were performed using NEMO_release_4.2.2. The simulation namelists and the supplementary routine implementing the EDMF parameterization are archived on Zenodo (https://doi.org/10.5281/zenodo.23536533, Piton, 2026). Instructions for accessing and downloading the model outputs are provided in the Zenodo repository. The GREP product at 1/4° resolution is available at https://doi.org/10.48670/moi-00024 (Copernicus Marine Service, 2026a). The OSTIA sea surface temperature product is available at https://doi.org/10.48670/moi-00165 (Copernicus Marine Service, 2026c), and the ARMOR and CORA-REP product at https://doi.org/10.48670/moi-00036 (Copernicus Marine Service, 2026b).

Supplement. The supplement related to this article is available online at https://doi.org/10.5194/os-22-3771-2026-supplement.

Author contributions. VP and RBB designed the methodology and the experiments, VP carried them out. VP carried the formal analysis. RBB, HG and CP developed the code. VP prepared the manuscript (original draft preparation) with contributions from all co-authors.

Competing interests. The contact author has declared that none of the authors has any competing interests.

Disclaimer. Publisher's note: Copernicus Publications remains neutral with regard to jurisdictional claims made in the text, published maps, institutional affiliations, or any other geographical representation in this paper. The authors bear the ultimate responsibility for providing appropriate place names. Views expressed in the text are those of the authors and do not necessarily reflect the views of the publisher.

Acknowledgements. We would like to thank the three reviewers (Baylor Fox-Kemper and two anonymous reviewers) and the handling editor (Julian Mak) for their valuable comments and suggestions, which have helped improve the presentation and discussion of our results.

Financial support. This work has received funding from the European Union's H2020 research and innovation program under grant agreement no. 101003536 (ESM2025 – Earth System Models for the Future). This study has also received funding from Agence Nationale de la Recherche – France 2030, as part of the PEPR TRACCS ANR IMPRESSION-ESM program under grant no. ANR-22-EXTR-0008.

Review statement. This paper was edited by Julian Mak and reviewed by Baylor Fox-Kemper, Bishakhdatta Gayen, and one anonymous referee.

References

Allende, S., Treguier, A. M., Lique, C., de Boyer Montégut, C., Massonnet, F., Fichefet, T., and Barthélemy, A.: Impact of ocean vertical-mixing parameterization on Arctic sea ice and upper-ocean properties using the NEMO-SI3 model, Geosci. Model Dev., 17, 7445–7466, https://doi.org/10.5194/gmd-17-7445-2024, 2024.

Behrens, E., Rickard, G., Morgenstern, O., Martin, T., Osprey, A., and Joshi, M.: Southern Ocean deep convection in global climate models: a driver for variability of subpolar gyres and Drake Passage transport on decadal timescales, J. Geophys. Res.-Oceans, 121, 3905–3925, https://doi.org/10.1002/2015JC011286, 2016.

Bellenger, H. and Duvel, J.-P.: An analysis of tropical ocean diurnal warm layers, J. Climate, 22, 3629–3646, https://doi.org/10.1175/2008JCLI2598.1, 2009.

Blanke, B. and Delecluse, P.: Variability of the tropical Atlantic Ocean simulated by a general circulation model with two different mixed-layer physics, J. Phys. Oceanogr., 23, 1363–1388, https://doi.org/10.1175/1520-0485(1993)023<1363:VOTTAO>2.0.CO;2, 1993.

Brodeau, L., Barnier, B., Gulev, S. K., and Woods, C.: Climatologically significant effects of some approximations in the bulk parameterizations of turbulent air–sea fluxes, J. Phys. Oceanogr., 47, 5–28, https://doi.org/10.1175/JPO-D-16-0169.1, 2017.

Revised vertical mixing parameters for the UK community standard configuration of the global NEMO ocean model, Met Office Hadley Centre Technical Note, 95,

207517, https://library.metoffice.gov.uk/Portal/Default/en-GB/RecordView/Index/207517 (last access: 1 April 2025), 2013.

Cheng, L., Trenberth, K. E., Palmer, M. D., Zhu, J., and Abraham, J. P.: Observed and simulated full-depth ocean heat-content changes for 1970–2005, Ocean Sci., 12, 925–935, https://doi.org/10.5194/os-12-925-2016, 2016.

Clément, L., Merckelbach, L., and Frajka-Williams, E.: Turbulent vertical velocities in Labrador Sea convection, Geophys. Res. Lett., 51, e2024GL110318, https://doi.org/10.1029/2024GL110318, 2024.

Copernicus Marine Service: Global Ocean Ensemble Physics Reanalysis, Marine Data Store (MDS) [data set], https://doi.org/10.48670/moi-00024, last access: 12 November 2026a.

Copernicus Marine Service: Global Ocean- In-Situ Near-Real-Time Observations, Marine Data Store (MDS) [data set], https://doi.org/10.48670/moi-00036, last access: 12 November 2026b.

Copernicus Marine Service: Global Ocean OSTIA Sea Surface Temperature and Sea Ice Analysis, Marine Data Store (MDS) [data set], https://doi.org/10.48670/moi-00165, last access: 12 November 2026c.

Couvreux, F., Hourdin, F., Williamson, D., Roehrig, R., Volodina, V., Villefranque, N., Rio, C., Ardouin, O., Salter, J., Bazile, E., Brient, F., Favot, R., Honnert, R., Lefebvre, M.-P., Madeleine, J.-B., Rodier, Q., and Xu, W.: Process-based climate model development harnessing machine learning: I. A calibration tool for parameterization improvement, J. Adv. Model. Earth Sy., 13, e2020MS002217, https://doi.org/10.1029/2020MS002217, 2021.

de Boyer Montégut, C.: Mixed layer depth over the global ocean: a climatology computed with a density threshold criterion of $0.03\,\mathrm{kg\,m^{-3}}$ from the value at the reference depth of 5 m, SEANOE [data set], https://doi.org/10.17882/98226, 2024.

de Boyer Montégut, C., Madec, G., Fischer Albert, S., Lazar, A., and Iudicone, D.: Mixed layer depth over the global ocean: an examination of profile data and a profile-based climatology, J. Geophys. Res.-Oceans, 109, C12003, https://doi.org/10.1029/2004JC002378, 2004.

Fer, I.: Near-inertial mixing in the central Arctic Ocean, J. Phys. Oceanogr., 44, 2031–2049, https://doi.org/10.1175/JPO-D-13-0133.1, 2014.

Fox-Kemper, B., Adcroft, A., Böning, C. W., Chassignet, E. P., Curchitser, E., Danabasoglu, G., Eden, C., England, M. H., Gerdes, R., Greatbatch, R. J., Griffies, S. M., Hallberg, R. W., Hanert, E., Heimbach, P., Hewitt, H. T., Hill, C. N., Komuro, Y., Legg, S., Le Sommer, J., Masina, S., Marsland, S. J., Penny, S. G., Qiao, F., Ringler, T. D., Treguier, A. M., Tsujino, H., Uotila, P., and Yeager, S. G.: Challenges and prospects in ocean circulation models, Front. Mar. Sci., 6, 65, https://doi.org/10.3389/fmars.2019.00065, 2019.

Frajka-Williams, E., Rhines, P. B., and Eriksen, C. C.: Horizontal stratification during deep convection in the Labrador Sea, J. Phys. Oceanogr., 44, 220–228, https://doi.org/10.1175/JPO-D-13-069.1, 2014.

Gan, B., Yu, J., Wu, L., Danabasoglu, G., Small, R. J., Baker, A. H., Jia, F., Jing, Z., Ma, X., Yang, H., and Chen, Z.: North Atlantic subtropical mode water formation controlled by Gulf Stream fronts, Nat. Sci. Rev., 10, nwad133, https://doi.org/10.1093/nsr/nwad133, 2023.

Garanaik, A., Pereira, F. S., Smith, L., Robey, R., Li, Q., Pearson, B., and Van Roekel, L.: A new hybrid mass-flux/high-order turbulence closure for ocean vertical mixing, J. Adv. Model. Earth Sy., 16, e2023MS003846, https://doi.org/10.1029/2023MS003846, 2024.

Gaspar, P., Gregoris, Y., and Lefevre, J. M.: A simple eddy kinetic energy model for simulations of the oceanic vertical mixing: tests at station Papa and long-term upper ocean study site, J. Geophys. Res., 95, 16179–16193, https://doi.org/10.1029/JC095iC09p16179, 1990.

Gent, P. R. and McWilliams, J. C.: Isopycnal mixing in ocean circulation models, J. Phys. Oceanogr., 20, 150–155, https://doi.org/10.1175/1520-0485(1990)0202.0.CO;2, 1990.

Giordani, H., Bourdallé-Badie, R., and Madec, G.: An eddy-diffusivity mass-flux parameterization for modeling oceanic convection, J. Adv. Model. Earth Sy., 12, e2020MS002078, https://doi.org/10.1029/2020MS002078, 2020.

Gordon, A. L.: Deep Antarctic convection west of Maud Rise, J. Phys. Oceanogr., 8, 600–612, https://doi.org/10.1175/1520-0485(1978)008<0600:DACWOM>2.0.CO;2, 1978. .

Grant, A. L. M.: Cloud-base fluxes in the cumulus-capped boundary layer, Q. J. Roy. Meteor. Soc., 127, 407–421, https://doi.org/10.1002/qj.49712757409, 2001.

Gülk, B., Roquet, F., Naveira Garabato, A. C., Bourdallé-Badie, R., Madec, G., and Giordani, H.: Impacts of vertical convective mixing schemes and freshwater forcing on the 2016–2017 Maud Rise polynya openings in a regional ocean simulation, J. Adv. Model. Earth Sy., 16, e2023MS004106, https://doi.org/10.1029/2023MS004106, 2024.

Hersbach, H., Bell, B., Berrisford, P., Hirahara, S., Horányi, A., Muñoz-Sabater, J., Nicolas, J., Peubey, C., Radu, R., Schepers, D., Simmons, A., Soci, C., Abdalla, S., Abellan, X., Balsamo, G., Bechtold, P., Biavati, G., Bidlot, J., Bonavita, M., De Chiara, G., Dahlgren, P., Dee, D., Diamantakis, M., Dragani, R., Flemming, J., Forbes, R., Fuentes, M., Geer, A., Haimberger, L., Healy, S., Hogan, R. J., Hólm, E., Janisková, M., Keeley, S., Laloyaux, P., Lopez, P., Lupu, C., Radnoti, G., Rosnay, P. de, Rozum, I., Vamborg, F., Villaume, S., and Thépaut, J.-N.: The ERA5 global reanalysis, Q. J. Roy. Meteor. Soc., 146, 1999–2049, https://doi.org/10.1002/qj.3803, 2020.

Heuzé, C., Ridley, J. K., Calvert, D., Stevens, D. P., and Heywood, K. J.: Increasing vertical mixing to reduce Southern Ocean deep convection in NEMO3.4, Geosci. Model Dev., 8, 3119–3130, https://doi.org/10.5194/gmd-8-3119-2015, 2015.

Holte, J., Talley, L. D., Gilson, J., and Roemmich, D.: An Argo mixed layer climatology and database, Geophys. Res. Lett., 44, 5618–5626, https://doi.org/10.1002/2017GL073426, 2017.

Houpert, L., Durrieu de Madron, X., Testor, P., Bosse, A., d'Ortenzio, F., Bouin, M. N., Dauss, H., Le Goff, H., Kunesch, S., Labastie, L., Mortier, L., and Raimbault, P.: Observations of open-ocean deep convection in the northwestern Mediterranean Sea: seasonal and interannual variability of mixing and deep water masses for the 2007–2013 period, J. Geophys. Res.-Oceans, 121, 8139–8171, https://doi.org/10.1002/2016JC011857, 2016.

Hourdin, F., Williamson, D., Rio, C., Couvreux, F., Roehrig, R., Villefranque, N., Musat, I., Fairhead, L., Binta Diallo, F., and Volodina, V.: Process-based climate model development harness-

ing machine learning: II. Model calibration from single column to global, J. Adv. Model. Earth Sy., 13, e2020MS002225, https://doi.org/10.1029/2020MS002225, 2021.

Hourdin, F., Ferster, B., Deshayes, J., Mignot, J., Musat, I., and Williamson, D.: Toward machine-assisted tuning avoiding the underestimation of climate change projections uncertainty, Sci. Adv., 9, eadf2758, https://doi.org/10.1126/sciadv.adf2758, 2023.

Kieke, D. and Yashayaev, I.: Studies of Labrador Sea Water formation and variability in the subpolar North Atlantic in the light of international partnership and collaboration, Prog. Oceanogr., 132, 220–232, https://doi.org/10.1016/j.pocean.2014.12.010, 2015.

Large, W. G., McWilliams, J. C., and Doney, S. C.: Oceanic vertical mixing: a review and a model with a non-local boundary layer parameterization, Rev. Geophys., 32, 363–403, https://doi.org/10.1029/94RG01872, 1994.

Lellouche, J.-M., Greiner, E., Bourdallé-Badie, R., Garric, G., Melet, A., Drevillon, M., Bricaud, C., Hamon, M., Le Galloudec, O., Renaudie, C., Cabanes, C., Tressol, M.-A., Greiner, F., Régnier, C., Benkiran, M., Drévillon, Y., and Le Traon, P.-Y.: The Copernicus Global 1/12° Oceanic and Sea Ice GLORYS12 Reanalysis, Front. Earth Sci., 9, 698876, https://doi.org/10.3389/feart.2021.698876, 2021.

Li, Q., Reichl, B. G., Fox-Kemper, B., Adcroft, A. J., Belcher, S. E., Danabasoglu, G., Grant, Alan L. M., Griffies, S. M., Hallberg, R., Hara, T., Harcourt, R. R., Kukulka, T., Large, W. G., McWilliams, J. C., Pearson, B., Sullivan, P. P., Van Roekel, L., Wang, P., and Zheng, Z.: Comparing ocean surface boundary vertical mixing schemes including Langmuir turbulence, J. Adv. Model. Earth Sy., 11, 3545–3592, https://doi.org/10.1029/2019MS001810, 2019.

Madec, G. and the NEMO System Team: NEMO Ocean Engine Reference Manual, Zenodo, https://doi.org/10.5281/zenodo.1464816, 2026.

Madec, G., Bell, M., Bourdallé-Badie, R., Chanut, J., Clementi, E., Coward, A., Drudi, M., Epicoco, I., Ethé, C., Iovino, D., Lea, D., Lévy, C., Lovato, T., Martin, N., Masson, S., Mathiot, P., Mele, F., Mocavero, S., Moulin, A., Müller, S., Nurser, G., Rousset, C., Samson, G., and Storkey, D.: NEMO ocean engine, in: Scientific Notes of IPSL Climate Modelling Center, Version v4.2, Zenodo, https://doi.org/10.5281/zenodo.6334656, 2022.

Marshall, J. and Schott, F.: Open-ocean convection: observations, theory and models, Rev. Geophys., 37, 1–64, https://doi.org/10.1029/98RG02739, 1999.

Masich, J., Kessler, W. S., Cronin, M. F., and Grissom K. R.: Diurnal cycles of near-surface currents across the tropical Pacific, J. Geophys. Res.-Oceans, 126, e2020JC016982, https://doi.org/10.1029/2020JC016982, 2021.

Morales Maqueda, M. A., Willmott, A. J., and Biggs, N. R. T.: Polynya dynamics: a review of observations and modeling, Rev. Geophys., 42, RG1004, https://doi.org/10.1029/2002RG000116, 2004.

Morel, A.: Optical modeling of the upper ocean in relation to its biogenous matter content (case I waters), J. Geophys. Res.-Oceans, 93, 10749–10768, https://doi.org/10.1029/JC093iC09p10749, 1988. .

Moum, J. N., Smyth, W. D., Hughes, K. G., Cherian, D., Warner, S. J., Bourlès, B., Brandt, P., and Dengler, M.: Wind dependencies of deep cycle turbulence in the equatorial cold tongues, J. Phys. Oceanogr., 53, 1979–1995, https://doi.org/10.1175/JPO-D-22-0203.1, 2023.

Pergaud, J., Masson, V., Malardel, S., and Couvreux, F.: A parameterization of dry thermals and shallow cumuli for mesoscale numerical weather prediction, Bound.-Lay. Meteorol., 132, 83–106, https://doi.org/10.1007/s10546-009-9388-0, 2009.

Perrot, M. and Lemarié, F.: Energetically consistent eddy-diffusivity mass-flux convective schemes: 2. Implementation and evaluations in an oceanic context, J. Adv. Model. Earth Sy., 17, e2024MS004616, https://doi.org/10.1029/2024MS004616, 2025.

Perrot, M., Lemarié, F., and Dubos, T.: Energetically consistent eddy-diffusivity mass-flux convective schemes: 1. Theory and models, J. Adv. Model. Earth Sy., 17, e2024MS004273, https://doi.org/10.1029/2024MS004273, 2024.

Piron, A., Thierry, V., Mercier, H., and Caniaux, G.: Gyre-scale deep convection in the subpolar North Atlantic Ocean during winter 2014–2015, Geophys. Res. Lett., 44, 1439–1447, https://doi.org/10.1002/2016GL071895, 2017.

Piton, V.: model namelists, code and ouputs access for EDMF, TKE+EVD, TKE+MLP+EVD simulations (NEMO4.2-SI3), Zenodo [code], https://doi.org/10.5281/zenodo.23536533, 2026.

Ramadhan, A., Wagner, G. L., Hill, C., Campin, J.-M., Churavy, V., Besard, T., Souza, A., Edelman, A., Ferrari, R., and Marshall, J.: Oceananigans.jl: Fast and friendly geophysical fluid dynamics on GPUs, J. Open Source Softw., 5, 2018, https://doi.org/10.21105/joss.02018, 2020.

Rio, C., Hourdin, F., Couvreux, F., and Jam, A.: Resolved versus parametrized boundary-layer plumes. Part II: continuous formulations of mixing rates for mass-flux schemes, Bound.-Lay. Meteorol., 135, 469–483, https://doi.org/10.1007/s10546-010-9478-z, 2010.

Rodgers, K. B., Aumont, O., Mikaloff Fletcher, S. E., Plancherel, Y., Bopp, L., de Boyer Montégut, C., Iudicone, D., Keeling, R. F., Madec, G., and Wanninkhof, R.: Strong sensitivity of Southern Ocean carbon uptake and nutrient cycling to wind stirring, Biogeosciences, 11, 4077–4098, https://doi.org/10.5194/bg-11-4077-2014, 2014.

Sathyendranath, S., Brewin, R. J. W., Brockmann, C., Brotas, V., Calton, B., Chuprin, A., Cipollini, P., Couto, A. B., Dingle, J., Doerffer, R., Donlon, C., Dowell, M., Farman, A., Grant, M., Groom, S., Horseman, A., Jackson, T., Krasemann, H., Lavender, S., Martinez-Vicente, V., Mazeran, C., Mélin, F., Moore, T. S., Müller, D., Regner, P., Roy, S., Steele, C. J., Steinmetz, F., Swinton, J., Taberner, M., Thompson, A., Valente, A., Zühlke, M., Brando, V. E., Feng, H., Feldman, G., Franz, B. A., Frouin, R., Gould, R. W., Hooker, S. B., Kahru, M., Kratzer, S., Mitchell, B. G., Muller-Karger, F. E., Sosik, H. M., Voss, K. J., Werdell, J., and Platt, T.: An Ocean-Colour Time Series for Use in Climate Studies: The Experience of the Ocean-Colour Climate Change Initiative (OC-CCI), Sensors, 19, 4285, https://doi.org/10.3390/s19194285, 2019.

Schott, F., Visbeck, M., Send, U., Fischer, J., Stramma, L., and Desaubies, Y.: Observations of deep convection in the Gulf of Lions, northern Mediterranean, during the winter of 1991/92, J. Phys. Oceanogr., 26, 505–524, https://doi.org/10.1175/1520-0485(1996)026<0505:OODCIT>2.0.CO;2, 1996.

Shay, T. J. and Gregg, M. C.: Convectively driven turbulent mixing in the upper ocean, J. Phys.

Oceanogr., 16, 1777–1798, https://doi.org/10.1175/1520-0485(1986)016<1777:CDTMIT>2.0.CO;2, 1986.

Siebesma, A. P., Bretherton, C. S., Brown, A., Chlond, A., Cuxart, J., Duynkerke, P. G., Jiang, H., Khairoutdinov, M., Lewellen, D., Moeng, C.-H., Sanchez, E., Stevens, B., and Stevens, D. E.: A large eddy simulation intercomparison study of shallow cumulus convection, J. Atmos. Sci., 60, 1201–1219, https://doi.org/10.1175/1520-0485(1996)026<0505:OODCIT>2.0.CO;2, 2003.

Soares, P. M. M., Miranda, P. M. A., Siebesma, A. P., and Teixeira, J.: An eddy-diffusivity/mass-flux parametrization for dry and shallow cumulus convection, Q. J. Roy. Meteor. Soc., 130, 3365–3383, https://doi.org/10.1256/qj.03.223, 2004.

Spall, M. A.: Dynamics of Downwelling in an Eddy-Resolving Convective Basin, J. Phys. Oceanogr., 40, 2341–2347, https://doi.org/10.1175/2010JPO4465.1, 2010.

Storkey, D., Blaker, A. T., Mathiot, P., Megann, A., Aksenov, Y., Blockley, E. W., Calvert, D., Graham, T., Hewitt, H. T., Hyder, P., Kuhlbrodt, T., Rae, J. G. L., and Sinha, B.: UK Global Ocean GO6 and GO7: a traceable hierarchy of model resolutions, Geosci. Model Dev., 11, 3187–3213, https://doi.org/10.5194/gmd-11-3187-2018, 2018.

Thomas, L. N. and Lee, C. M.: Intensification of ocean fronts by down-front winds, J. Phys. Oceanogr., 35, 1086–1102, https://doi.org/10.1175/JPO2737.1, 2005.

Tomita, H., Kutsuwada, K., Kubota, M., and Hihara, T.: Advances in the estimation of global surface net heat flux based on satellite observation: J-OFURO3 V1.1, Front. Mar. Sci., 8, 612361, https://doi.org/10.3389/fmars.2021.612361, 2021.

Treguier, A. M., de Boyer Montégut, C., Bozec, A., Chassignet, E. P., Fox-Kemper, B., McC. Hogg, A., Iovino, D., Kiss, A. E., Le Sommer, J., Li, Y., Lin, P., Lique, C., Liu, H., Serazin, G., Sidorenko, D., Wang, Q., Xu, X., and Yeager, S.: The mixed-layer depth in the Ocean Model Intercomparison Project (OMIP): impact of resolving mesoscale eddies, Geosci. Model Dev., 16, 3849–3872, https://doi.org/10.5194/gmd-16-3849-2023, 2023.

Treguier, A.-M., Held, I. M., and Larichev, V. D.: Parameterization of quasigeostrophic eddies in primitive equation ocean models, J. Phys. Oceanogr., 27, 567–580. https://doi.org/10.1175/1520-0485(1997)027<0567:POQEIP>2.0.CO;2, 1997.

Våge, K., Pickart, R. S., Thierry, V., Reverdin, G., Lee, C. M., Petrie, B., Agnew, T. A., Wong, A., and Ribergaard, M. H.: Surprising return of deep convection to the subpolar North Atlantic Ocean in winter 2007–2008, Nat. Geosci., 2, 67–72, https://doi.org/10.1038/ngeo382, 2009.

Van Roekel, L. P., Adcroft, A. J., Danabasoglu, G., Griffies, S. M., Kauffman, B., Large, W. G., Levy, M., Reichl, B. G., Ringler, T., and Schmidt, M.: The KPP boundary layer scheme for the ocean: Revisiting its formulation and benchmarking one-dimensional simulations relative to LES, J. Adv. Model. Earth Syst., 10, 2647–2685, https://doi.org/10.1029/2018MS001336, 2018.

Vancoppenolle, M., Rousset, C., Blockley, E., Aksenov, Y., Feltham, D., Fichefet, T., Garric, G., Guémas, V., Iovino, D., Keeley, S., Madec, G., Massonnet, F., Ridley, J., Schroeder, D., and Tietsche, S.: SI3, the NEMO Sea Ice Engine, Zenodo, https://doi.org/10.5281/zenodo.7534900, 2023.

Vreugdenhil, C. A. and Gayen, B.: Ocean convection, Fluids, 6, 360, https://doi.org/10.3390/fluids6100360, 2021.

Wenegrat, J. O. and McPhaden, M. J.: Dynamics of the surface layer diurnal cycle in the equatorial Atlantic Ocean (0°, 23° W), J. Geophys. Res.-Oceans, 120, 563–581, https://doi.org/10.1002/2014JC010504, 2015.

Woolnough, S. J., Vitart, F., and Balmaseda, M. A.: The role of the ocean in the Madden–Julian Oscillation: implications for MJO prediction, Q. J. Roy. Meteor. Soc., 133, 117–128, https://doi.org/10.1002/qj.4, 2007.

Yashayaev, I. and Loder, J. W.: Further intensification of deep convection in the Labrador Sea in 2016, Geophys. Res. Lett., 44, 1429–1438, https://doi.org/10.1002/2016GL071668, 2017.

Zhang, J., Schmitt, R. W., and Huang, R. X.: Sensitivity of the GFDL modular ocean model to parameterization of double-diffusive processes, J. Phys. Oceanogr., 28, 589–605, https://doi.org/10.1175/1520-0485(1998)028<0589:SOTGMO>2.0.CO;2, 1998.

Zhang, Q., Liu, B., Li, S., and Zhou, T.: Understanding models' global sea surface temperature bias in mean state: from CMIP5 to CMIP6, Geophys. Res. Lett., 50, e2022GL100888, https://doi.org/10.1029/2022GL100888, 2023.

Zhu, Y. and Zhang, R.-H.: A modified vertical mixing parameterization for its improved ocean and coupled simulations in the tropical Pacific, J. Phys. Oceanogr., 49, 21–37, https://doi.org/10.1175/JPO-D-18-0100.1, 2019.